Measuring gross Beryllium erosion with visible cameras in JET Ohmic limiter plasmas

E. de la Cal[1], U. Losada[1], I. Balboa[2], D. Borodin[3], I. Borodkina[3], S. Brezinsek[3], P. Carvalho[2], T. Dittmar[3], D. Douai[4], A. Huber[2], V. Huber[2], J. Karhunen[5], A. Manzanares[1], A. Shaw[2], S. Silburn[2] , E. R. Solano[1] and JET contributors[*]

[1] Laboratorio Nacional de Fusión, CIEMAT, Av. Complutense 40, E-28040 Madrid, Spain

[2] CCFE Fusion Assoc., Culham Science Centre, Abingdon, OX14 3DB, UK

[3] Forschungszentrum Jülich GmbH, Institut für Energie- und Klimaforschung-Plasmaphysik, D-52425, Jülich, Germany

[4] CEA, IRFM, F-13108 Saint-Paul-lez-Durance, France

[5]Aalto University, Department of Applied Physics, 02150 Espoo, Finland

[*]See the author list of "X. Litaudon *et al* 2017 *Nucl. Fusion* 57 102001"

E-mail: e.delacal@ciemat.es

The figures contain embedded videos that cannot be visualised with the present pdf file. You can download the figure files including the videos in:

http:/www-fusion.ciemat.es/fileshare/doc_exchange/JET%202021%20delaCal/Yeff_Be_Figures%20%281%29.pptx

Abstract

Two visible cameras with the same wide-angle view have been used to study the gross Beryllium erosion in JET Ohmic limiter plasmas. An absolutely calibrated spectroscopy system employed in the past for the same object was used to infer quantitatively the camera photon fluxes and validate the results. A simplified method to extract the effective sputtering yield from the quotient of the measured radiances of the D_α- and the Be II line at 527 nm was applied. The obtained results are in reasonably good agreement with those already published. The main benefit of using cameras is that a global view of the plasma-wall interaction surfaces of the whole vessel is monitored and the different sources and their wetted areas can be identified and quantified. Also, the measurement of the particle flux distributions can be used for validation of 3-dimensional erosion-transport codes.

1. Introduction

The ITER Plasma Facing Components (PFCs) will consist of beryllium (Be) bulk limiters, Be-coated wall panels and a divertor of tungsten (W) tiles [see e.g. 0]. Due to the much longer duty cycle compared with today's fusion devices, extrapolation from actual experimental studies try to anticipate in how much the lifetime of ITER's PFCs is limited by plasma erosion [see e.g. 1-5]. Unfortunately, these simulations based on the material erosion yields and edge transport plasma modelling, have large incertitude and experimental observations are necessary for their validation. Besides the erosion problem of the Be components, a major concern is the formation of Be co-

deposits due to the sputtered, transported and re-deposited atoms that will be the dominant T retention mechanism [see e.g. 6, 7]. Additionally, Be will be the dominant intrinsic impurity in ITER plasmas arriving to the tungsten (W) divertor which will increase its erosion and its concentration in the confined plasma affecting negatively the reactor's global performance [see e.g. 8-10]. Despite the importance of these issues for ITER, experimental Be erosion studies are scarce and impurity transport codes to simulate erosion and re-deposition studies need from this input for validation.

JET, with its ITER-like metallic wall (ILW) is provided with Be limiters that protect the inner and outer first wall and a W divertor. In fact, it is the only fusion device operating with Be and thereby the sole where its erosion can be studied in situ and moreover with similar reactor geometry and edge plasma conditions as ITER. Dedicated erosion experiments were done in the past where the plasma and Be fluxes were measured using spectroscopic means. In [11] the so-called Be effective sputtering yield Y^{eff}_{Be} (see later) was studied using a plasma density scan to vary the impact energies of impinging deuterium using a spectroscopy system observing a discrete spot at the inner mid-plane of a limiter. This yield is directly linked to the gross erosion rate and does not take into account re-deposition. In [12], using the same system, the physical and chemical branches of the Be sputtering yields were measured by varying the limiter surface temperature and the plasma density. These data were used for interpreting Be migration studies including post mortem-analysis [13, 14] and to validate the results obtained with the impurity transport code ERO [15, 16].

The motivation of the present work is to provide further experimental information on Be gross erosion in JET using two visible cameras. Both cameras measure the plasma and Be fluxes with the same wide-angle view of JET's chamber including inner and outer limiters as well as the divertor. Thus, the main advantage with respect to the spectroscopy system used in the past is to get a global view of the fluxes from the plasma-wall interaction surfaces of the whole vessel. Thereby all the regions of interest can be monitored and the different sources and their wetted areas can be identified. The measurements can be also used for validation of 3 dimensional erosion-transport codes such as ERO.

In the future, ITER will be equipped with a large set of wide-angle infrared and visible cameras outside the Bio-shield that image the surface and plasma emission from 4 mid-plane ports to routinely monitor the in-vessel components. The main function of this diagnostic is the protection of the PFCs protection, but secondary roles with additional cameras will include scientific purposes [17, 18]. Soon the final light line splitting and opto-mechanical design in the port cells outside the Bio-shield, including the filtering capacity and camera specifications will be decided [19, 20]. The use of visible cameras for physics studies is gaining relevance, for example in JET for tungsten erosion studies [21], for divertor plasma characterisation [22] or for fast phenomena studies such as disruptions, pellet injection or ELMs [23]. The present Be erosion study is a new example of the possibility of using such "scientific" cameras (with e.g. filtering capacity, Image Intensification and high-recording speed) for complementary functions of this ITER diagnostic.

In the present work, we first describe the used visible camera system and its calibration to measure the plasma and Be fluxes. Than we explain how the gross or effective Be erosion yield Y^{eff}_{Be} is inferred using the well-known S/XB method that relates photon and particle fluxes (see later) in a simplified way. We take here advantage of the relatively small variation of the ratio of the S/XB coefficients with the expected edge plasma density and temperatures n_e and T_e for the Ohmic limiter plasmas here analysed and propose to fix this ratio as a constant. After describing the errors that must be assumed doing this, the method to get Y^{eff}_{Be} is validated with data of the spectroscopy system from past-published experiments [12]. Once this is done, recent camera data are analysed in the same way and compared to those of the spectrometer looking at the inner limiter. This is shown for different plasma configurations and examples are given explaining step by step the analysis starting from the camera video-clips. The measured Y^{eff}_{Be} values are in good agreement with the prior art. Finally, we make an equivalent analysis at the limiters for L-H dithering diverted plasma and discuss the larger uncertainties and how these could be reduced.

2. Experimental

The here used camera system called KLDT is installed outside the JET biological shield and receives the image from an equatorial port after being transported along a path of more than 10 m. This was done to allow its operation at high neutron and Gamma radiation levels as in the actual D-T campaign. The in-vessel optics images the JET vacuum chamber with a wide-angle view composed from two separate lines, a lower and an upper branch, each viewing half of the machine [2.1]. Both are then combined to form a full intermediate image after the port window, which is finally transported via a mirror based optical relay lens towards the camera system [2.2]. The light beam is split there to four cameras: a NIR protection camera, an IR thermography camera and the here used visible "Spectroscopy camera" with filtering capacity and the visible "High speed- or Fast-camera". The cameras view is shown in **figure 2.1** where typical coloured emission regions have been superposed on the picture to show the here analysed plasma surface interaction regions: an inner and an outer limiter and the upper inner divertor (for calibration issues). The angles between the camera lines of view and the surface normals of these regions are indicated. Also shown are the lines of view and the observed spots of the two spectroscopy systems, KS3H and KS3D, used in the present work and described below. The frontier between the upper and lower image branches can be distinguished near the torus mid-plane.

The "Spectroscopy camera" has a 512 x 512, 16 μm, pixels Electron Multiplying CCD sensor and is used here with a 1 nm bandwidth interference filter centred at the Be II 527.1 nm atomic line. The signal level can be amplified, although for the here analysed plasmas the gain level only was varied between +/- 20%. The recording speed was generally set to 80 frames per second (fps) and the exposure time τ_{exp} was typically set between 1 and 5 ms. The visible "Fast-camera" is a Photron APX-RS with a CMOS sensor of 1024 x1024, 17 μm pixels able to record $3x10^3$ fps at full frame and up to $2.5x10^5$ fps at reduced active sensor size. The maximum recording time is limited to 2 GB so that the video length depends on both the Region Of Interest (ROI) size and the

frame rate but can be divided in separated sub-intervals. The visible light is unfiltered, but as shown later, it mainly is comprised of D_α-line emission [2.3]. Some applications of the two existing Fast cameras in JET can be found in [23]. Both cameras were cross-calibrated against the absolute radiance measurements of the visible spectroscopy system described below. The procedure is explained in the separate appendix. The videos are visualized and analysed with the software framework JUVIL [2.4], which was specifically created to handle all the cameras of the JET viewing system.

The spectroscopy system used here and in the past [11, 12] to measure the Be erosion collects light from a spot at the border of a limiter at the near SOL close to the inner mid-plane (see **figure 2.1, KS3H**). The light is transported to a spectrometer system and different lines such as the D_γ and BeII (527.1 nm) are routinely acquired with a time resolution of 100 ms. The other spectroscopy system used for the calibration of the cameras views the divertor with a fiberscope along 20 chords from an upper vertical port of the machine (see **figure 2.1, KS3D**). The light is transported to the measurement cabinet where it is filtered using narrow bandwidth filters centred at different characteristic atomic lines such as the here used D_α- and the Be II (527.1 nm) lines and measured with photomultiplier tubes at a frequency of 100 kHz.

3. A simplified S/XB method to measure the effective sputtering yield Y^{eff}_{Be}

The effective sputtering yield of a D plasma impinging on a Be surface Y_{Be}^{eff} is defined as:

$$(3.1) \quad Y_{Be}^{eff} = \frac{F_{Be}^{out}}{F_D^{in}},$$

where F_{Be}^{out} is the Be out-flux sputtered from the surface produced by the D plasma in-flux F_D^{in}. The Be out-flux has two sputtering precursors from the plasma, the majority impinging D flux (the fuel) and the impurity flux, mainly Be in JET, that causes the so-called self-sputtering. In fact, equation (3.1) can be rewritten as [11]:

$$(3.2) \quad Y_{Be}^{eff} = \frac{Y_{Be>D}}{1 - xY_{Be>Be}},$$

where $Y_{Be>D}$ is the Be sputtering yield due to D, $Y_{Be>Be}$ the self-sputtering yield and x is the Be fraction onto the surface. The major contribution of $Y_{Be>D}$ is physical sputtering, the other Chemical Assisted Physical Sputtering (CAPS) that produces the volatile molecule BeD. CAPS has been measured in JET to contribute up to 30% for the base operational limiter temperature of T ≈ 200 ^{o}C and decreases as the surface temperature increases, vanishing for T > 500 ^{o}C [12]. In the present work the global yield is measured without distinguishing both mechanism.

To retrieve experimentally Y_{Be}^{eff} in JET, spectroscopic means were used in the past applying the well-known S/XB method [11, 12]. This method relies in converting the measured photon radiances L of a specific atomic line to the corresponding particle fluxes F of the emitting atom when entering into the plasma and following equation is used [3.1]:

(3.3) $F = 4\pi\, A\, S/XB\, L$,

where A is the observing area and S/XB is the so called inverse photon efficiency or number of ionization events per photon of a specific atomic line. S/XB, that depends locally on T_e and n_e along the emission layer at the edge plasma, is generally estimated using atomic Collisional-Radiative models. In ionizing plasma conditions as here (T_e > 5 eV) recombination reactions can be neglected. The S/XB coefficients of many fusion plasma relevant atomic lines can be found in the ADAS database [3.2] and are shown for the D_α and BeII at 527 nm lines in **figure 3.1a** as a function of T_e for $n_e = 0.5 \times 10^{19}$ and 2×10^{19} m^{-3} and in **figure 3.1b** as a function of n_e for T_e = 30 and 100 eV. These lines are the ones used in [11, 12] to measure Y_{Be}^{eff} and also in the present work using the equation:

$$(3.4) \quad Y_{Be}^{eff} \approx \frac{(S/XB)_{BeII}\, L_{BeII}}{(S/XB)_{D\alpha}\, L_{D\alpha}} \approx R_{S/XB} \frac{L_{BeII}}{L_{D\alpha}} \,.$$

Here we have introduced the ratio $R_{S/XB} = (S/XB)_{BeII} / (S/XB)_{D_\alpha}$ and will be analysed later in detail after a discussion on the S/XB determination. The assumption that the plasma in-flux onto the limiters F_D^{in}, mainly D^+ ions, is approximately equal to the re-emitted D (neutral) atom flux that emit the D_α photons is justified by the fact that the Recycling coefficient $R \approx 1$.

Unfortunately, there are generally significant uncertainties when applying the S/XB method due to different reasons and approximations must be taken. In most cases, the main uncertainty comes from the fact that the radiance L is a line-integrated measurement along the plasma edge emission layer and therefore a mean S/XB must be estimated since generally the n_e-, the T_e- and the emission-radial profiles are unknown. In other words, **equations 3.3 and 3.4** use on one side the integrated emission radiances, which are a direct experimental measurement, but on the other side the S/XB coefficients, which are approximated to a mean or integrated $\langle S/XB(n_e, T_e) \rangle$ value along the line of view weighted by the emission intensity profile across the plasma. Another difficulty appears when measuring the D emission, as the D_α–line here, because of the complexity of the atomic collisional paths involved in the line radiation. For example the molecular branch that becomes ionised without emitting at the corresponding line is generally included in the S/XB coefficient and may generate an undercounting of this coefficient [3.3, 3.4]. In order to minimise this uncertainty, besides characterising the n_e and T_e near the emission layer as well as possible, a possible solution is to use a neutral transport code such as EIRENE to get S/XB taking into account all the important molecular reactions [3.5]. The advantage is that the line integrated value of the product of the radiance L and the local S/XB value along the viewing chord can be directly obtained by the code. For the case of the edge plasma studied in [3.5], the $(S/XB)_{D_\alpha}$ value calculated nearest to the recycling surface, where

the molecular density dominates over the atomic one, was a factor of two larger than at deeper plasma regions, in agreement with the experimental results of [3.4]. Globally, the line-integrated value weighted along the emission profile gave about a 25% higher value than the pure atomic branch in the region where molecules are absent.

Concerning the first uncertainty, fortunately in many cases, the n_e and T_e dependence of S/XB is rather small. For the here analysed Ohmic limiter plasmas, most of the emission region is expected to come from the first 5 - 10 centimetres inside the Last Closed Flux Surface (LCFS) and there Langmuir probe measurements in JET were reported to be of $25 < T_e$ (eV) < 200 eV and $5x10^{18} < n_e$ (m^{-3}) $< 2x10^{19}$ [3.6, 3.7]. In this parameter ranges the S/XB coefficients variations are relatively weak. Moreover, for the estimation of Y_{Be}^{eff} using equation (3.4) only the value of the ratio $R_{S/XB}$ is used, which as can be seen from **figures 3.2a and 3.3b** has even a smaller n_e- and T_e-dependency. Taking advantage of this, if a constant value of $R_{S/XB} = 2.4$ is taken, the maximum error in the above plasma parameter range is estimated to be of about +/- 25%.

Concerning the second uncertainty, we have to correct for the molecular D branch that the $(S/XB)_{D_\alpha}$ from ADAS does not account for. In the present work the ADAS $(S/XB)_{D_\alpha}$ coefficient has been increased arbitrarily by 30% to compensate for this. With this correction we finally fix the S/XB ratio to a value of $R_{S/XB} = 1.8$. In the next section it will be shown, that with this approximation a relatively good agreement with prior results are obtained. Anyway, since the $R_{S/XB}$ dependence with T_e and n_e can be estimated, its value can be corrected in future quite simply if these edge plasma parameters are narrowed down as will be discussed at the end of the paper.

4. Results

Figures 4.1 show prior Y^{eff}_{Be} measurements in Ohmic plasmas using the described spectroscopy system collecting light coming from an inner Be lmiter at the mid-plane, **a)** is from [11] and the experimental points of **b)** from [12]. These Y^{eff}_{Be} measurements where later used to validate the impurity transport code ERO code [4.1]. The clear Y^{eff}_{Be} decrease with plasma density in [12] was measured for a series of repetitive discharges with same magnetic field and plasma current where the density was slowly increased from pulse to pulse. This was attributed to the decrease of T_e at the limiters and thereby of the impinging ion energy when the average plasma density rises. A similar trend of the yield with the plasma density was also observed in [11] although with a larger dispersion and generally with higher absolute values.

4.1 Validation of the simplified S/XB method

Before analysing the camera data and in order to check for the validity of the proposed simplified S/XB method, the measured radiance data of [12] were analysed here again but using **equation (3.4)** with $R_{S/XB} = 1.8$. In this prior work, two different set of Ohmic limiter plasmas were studied: a first one with repetitive discharges to heat up the Be limiters and study the effect of the temperature on the Chemical Assisted Physical Sputtering (CAPS) and a second one with density scans to vary the edge plasma T_e and thereby the impinging ion energy on the limiters. Different atomic lines were measured using the spectroscopy system to infer the D and Be fluxes and also to

get information on the edge plasma parameters. For this, the ratio of two atomic Be I line radiances at 467 and 436 nm with a relatively week n_e-dependency was used two obtain information on T_e. The radiances of these lines were retrieved here again from the database and their ratio is shown in **figure 4.2** as a function of the line integrated density $n_e dl$ ($\langle n_e \rangle \approx n_e dl$ / 2.2 m for typical JET limiter plasmas) for the n_e-scan (JET Pulse Number or JPN #80319 - #80323) and for two plasmas of the "limiter heating" experiment (marked with circles are JPN #82592, the first one of the series and JPN #82626, the last one). The values were taken at the same time as in [12], 10 seconds after plasma start-up. The obtained line ratio increases with plasma density from about 2.1 to 2.4. An increase of this ratio is in agreement with a local raise of n_e and/or a decrease in T_e (see figure 3 in [12]). Unfortunately, with this low-varying line ratio and without an independent measurement of n_e, there is a rather large uncertainty to retrieve T_e. It is to be noted that the two points corresponding to the "Limiter heating" plasmas, that had different magnetic field and plasma current, do not follow the same tendency with $n_e dl$ as the others. **Figure 4.3a** shows for these plasmas the radiance measurements of the spectroscopy system of the Be II (527 nm) and D_γ lines as a function $n_e dl$. Except for the lowest n_e, both show a linear increase with the plasma density. The raise of L_{BeII} at very low densities clearly visible in the figure was attributed to the increase of Be self-sputtering that becomes strongly enhanced at sufficiently high ion energies. The major deviation from this linear fit is the measurement of L_{BeII} of discharge #82626 that corresponds to the one with the highest limiter surface temperature T ≈ 500 ^oC where CAPS was demonstrated to completely vanish.

As explained in section 2, the spectroscopy system looking horizontally to an inner limiter does not routinely acquire the D_α line, but instead the D_γ one. However, for the here analysed ionizing plasma conditions both lines should be proportional and the relation $D_\alpha \approx 30\ D_\gamma$ is generally used [see e.g. 11]. Using this relation Y_{Be}^{eff} was inferred using **equation (3.4)** with $R_{S/XB} = 1.8$. **Figure 4.3b** shows the result for this data set. The run-out of the yield for the lowest densities (yellow strip) is clearly visible as already obtained in the past. **Figure 4.3c** is a zoom of the same for $n_e dl \geq 4 \times 10^{19}$ m^{-2} where the obtained Y_{Be}^{eff} decreases from about 0.27 to 0.12 when increasing the plasma density. Schematically plotted are the smoothed fit of our data (blue line), the past-published results shown in **figure 4.1b** from [12] (yellow line) and the Y_{Be}^{eff} domain obtained in [11] (orange area). The here-obtained Y_{Be}^{eff} values are in good agreement with those of the prior published data and have the expected similar decreasing behaviour with the plasma density as those of the past. They are lower than those of [11], but are about a 25% higher compared to the values of [12] for $n_e dl \approx 4 \times 10^{19}$ m^{-2} This deviation increases up to a factor of two for the highest plasma densities. The reason of this increasing overestimation of the yield as the plasma density is raised can be attributed partly to the decrease of $R_{S/XB}$ due to a plasma edge n_e and T_e decrease (see figures 3.2). Finally it is to be noted that the effect of the CAPS contribution of about 30% to the total yield Y_{Be}^{eff} for the "low" respect to the "high" surface temperature has been also obtained here in agreement with [12].

4.2 Measuring Y^{eff}_{Be} with cameras

4.2.1 Ohmic inner limiter plasma with density ramp

Many Ohmic limiter plasmas from last experiment campaigns have been analysed in the frame of the present work and some examples will be shown next. We have tried whenever possible to compare the camera measurements with those of the spectroscopy system using the same simplified S/XB method to obtain Y^{eff}_{Be} . The here studied plasmas include firstly recent dedicated Be erosion experiments similar to those of [12] and also other Ohmic limiter scenarios. These are the limiter plasma start-up phase common to all JET plasmas and also the so-called limiter "Cycling" discharges used for wall cleaning. Unfortunately, the number of plasmas where both cameras, especially the Fast camera, had the correct settings to monitor the limiters are scarce.

The first initially surprising observation was that the measured Y^{eff}_{Be} did not always scale inversely with the average plasma density and thanks to cameras the reason for this could be unravelled as will be shown next. In f**igure 4.4** is embedded a video-clip recorded with the Be II filtered camera (80 fps, τ_{exp} = 3 ms), where after the plasma break-down and build-up at the outer limiters till its complete expansion, a density-ramp was produced by continuously increasing the gas fuelling with the plasma leaning at the inner limiters till a MARFE triggered the pulse stop (JET Pulse Number or JPN #95790). The time traces of the average plasma density $<n_e>$ and the Be II and D_γ radiances measured by the spectroscopy system are plotted in **figure 4.5a [COMMENT *]**. The n_e-ramp at the inner limiter begins at t ≈ 45.5 s ($<n_e>$ ≈ 1.2 x10^{19} m^{-3}) till t ≈ 50 s ($<n_e>$ ≈ 3.5 x10^{19} m^{-3}) where the MARFE begins. **Figure 4.5b** shows the Y^{eff}_{Be} time evolution estimated using **equation (3.4)** with the spectroscopy system data. The ratio of the two atomic Be I line radiances at 467 and 436 nm is also plotted, showing a slow continuous increase during the n_e-ramp from about 2.7 to 3.2. This indicates a continuous local n_e rise and/or T_e decrease at the plasma edge as expected. During the plasma build-up at the inner limiter (43 s < t < 44.5 s), the D_γ-emission is extremely low compared to the Be II and Y^{eff}_{Be} runs out to very high values > 1. Later Y^{eff}_{Be} decreases as expected from a value of about 0.3 to about 0.15 at $<n_e>$ ≈ 1.5 x10^{19} m^{-3}. Afterwards, although the density increases, unexpectedly Y^{eff}_{Be} stays constant and even raises to a value of 0.22 till $<n_e>$ ≈ 2.5 x10^{19} m^{-3}. Only at the final part of the n_e-ramp, the yield continues its decrease and finally, when the MARFE starts, the Be fluxes strongly fall. This varying Y^{eff}_{Be} behaviour during the n_e-ramp does not follow the simple trend with plasma density as in the section before. A possible explanation of this can be found looking to the Be II camera video in detail. **Figure 4.6** shows four frames at different times marked with yellow arrows in **figure 4.5** with the interaction region at the mid-plane of the analysed limiter. The scales are adapted to better visualize the emission maxima. It can be seen that the plasma-surface region with strongest interaction moves downwards as $<n_e>$ increases till t = 48 s, than its stays fixed for the rest of the n_e-ramp. The magnetic field reconstruction also shows for this period (t =

46.5 s – 48 s) a global downwards plasma movement. To show this in more detail, the time evolutions of the camera signal intensity for the marked ROIs were analysed. They are plotted in **figure 4.7**. The blue curves correspond to the maximum (dark blue) and mean (light blue) of the intensity of the large blue ROI embracing the whole limiter region where the main interaction takes place. The intensity at these ROIs increases continuously and is not affected by the exact Strike Point (SP) location. The red ROI corresponds to the small red rectangular ROI at the inner mid-plane where the spectroscopy approximately system looks at. The intensity time trace there shows a similar behaviour as that of the radiance measured by the spectrometer. It can be deduced that from t = 46 s to 47 s the radiances measured by the spectroscopy system raise continuously because n_e increases but also because the SP is approaching the observation spot. From t = 47.2 s to 48 s the intensities stop raising because even if n_e increases, the SP has already passed the observation spot and is moving away downwards. The increase of Y^{eff}_{Be} during this period is not understood. Afterwards the SP stays at the same position and the radiances continue its increase as n_e does and Y^{eff}_{Be} starts to decrease due to the T_e decrease. Note that the emission pattern at the end has two maxima, something that may be attributed to some irregularity in the Be surface at this limiter.

All this shows that the local emission coming from the discrete small area where the spectroscopy system is looking at is sensible to the exact spatial plasma-surface interaction distribution where different fluxes and local plasma parameters may change. This fact should be taken into account when interpreting the spectroscopy data and attention should be paid when linking its measurements to the real erosion field at the limiters and also to global plasma parameters as $<n_e>$.

4.2.2 Ohmic outer limiter plasma

The same plasma of the example before was changed after the MARFE to an outer limiter configuration as shown in the video embedded in **figure 4.6**. The first part of this clip is from the Be II camera and the final part from the Fast camera at 2x10 fps and τ_{exp} = 50 μs that was monitoring the outer walls for a brief period. A zoom of the analysed outer limiter is depicted in **figure 4.7** from a) the Be II camera and b) the Fast camera at the same instant. The average intensity over 10 frames within the same marked ROIs was calculated for both and is given in the figures. From these values divided by their respective exposure times and using the calibration factors the radiances were obtained: $L_{D_\alpha} \approx 3.4 \times 10^{15}$ ph s^{-1} cm^{-2} sr^{-1} and $L_{BeII} \approx 2.9 \times 10^{14}$ ph s^{-1} cm^{-2} sr^{-1}. Applying **equation (3.4)** with $R_{S/XB} = 1.8$ we obtain a gross erosion yield $Y^{eff}_{Be} \approx$ 0.16. This value was measured with a plasma density of $<n_e> \approx 4 \times 10^{19}$ m^{-3} and is similar to that obtained at the inner limiter of the same plasma at the highest density. As will be discussed later when analysing a "Cycling" plasma, it is to be noted that the areas where most of the plasma-limiter interaction takes place, the so-called "wetted areas", are sensibly smaller at the outer compared to the inner limiters, while the D_α and Be II emission fluxes larger.

4.2.3 Ohmic limiter plasma start-up

In JET generally, plasmas are build-up with a limiter configuration at the low field side as displayed in **figure 4.10** before going to the diverted configuration and additional heating phase. A similar plasma start-up scenario is also foreseen for ITER. The video-clip embedded in **figure 4.11** shows this initial phase of a typical JET plasma (JPN #97809) as seen with both cameras. The first part of the video was recorded with the Fast camera at moderate speed (200 ms at 10^3 fps and τ_{exp} = 1 ms) and the second part with the Be II camera (2s at 80 fps and τ_{exp} = 3 ms). One frame from each camera at the same instant with the plasma Separatrix touching the outer limiters is shown in **figure 4.12.** The selected ROIs contain the main plasma-surface interaction region coinciding with the emission at the observed limiter. They cover more than 80% of the total radiation from the limiter. The time traces of the mean values at these ROIs are plotted in **figure 4.13** together with that of the average plasma density. Using the calibration factors and **equation A.1** the camera signals are converted to radiances (**figure 4.14)** and finally Y_{Be}^{eff} is calculated using **equation (3.4)** with $R_{S/XB} = 1.8$. As can be seen, its value decreases from about $Y_{Be}^{eff} \approx 0.25$ to 0.08 as the plasma average density increases from about 0.4 to 1.5 x10^{19} m^{-3}. Interestingly, here we do not see the Be-sputtering run-out and the yield is lower than expected for this low-density regime compared to those analysed in **figure 4.3b**. This can be attributed to the fact that during the first seconds during the plasma build-up phase, the plasma electron temperature T_e as measured with Thomson scattering is much colder, about a factor of two in the centre, than later for same density. Correspondingly, it can be expected that in this initial phase the ions impinging at the limiters have lower energies compared to limiter plasmas with same low densities but already in thermal equilibrium.

4.2.4 Ohmic Limiter cycling plasma in Hydrogen

In JET, the so-called "Limiter cycling" discharges are Ohmic plasmas where the strike point of the Separatrix rotates several times around the inner and outer limiters. The objective is the conditioning of the first wall. **Figure 4.15** shows the magnetic configurations at two time instants of the here analysed "Cycling" plasma (JPN #98739) touching the inner and outer limiters at the mid-planes. The video-clip embedded in **figure 4.16** recorded with the Be II filtered camera (80 fps, τ_{exp} = 3 ms) shows one cycling period during this discharge. It belongs to a recent Hydrogen (H) JET campaign for isotope studies. The goal of analysing this plasma is to compare the Y_{Be}^{eff} yield measurement with the cameras and the spectroscopy system at the inner limiter and also the inner respect to the outer limiter yield values as obtained for similar densities thanks to the cameras wide-angle view.

Figure 4.17 shows the time traces of the average line density $n_e dl$ and the BeII and H_γ radiances as measured by the spectroscopy system looking to the inner mid-plane. During the phases where the radiances increase, the plasma is leaning at the inner limiters (green stripes) and oppositely when it interacts at the outer limiters. In a similar

way as estimated in **section 4.1**, with $L_{H_\alpha} \approx 30\ L_{H_\gamma}$ and $R_{S/XB} = 1.8$, we get a yield of $Y_{Be}^{eff} \approx 0.08$ near the emission maxima.

On the other side the photon fluxes and yield was estimated using the cameras at two time instants marked in **figure 4.17** with dashed yellow lines, one with the plasma interacting at the outer and the other at the inner limiters. **Figures 4.18 a) and b)** display the average images over the frames along 100 ms of both camera videos at t = 50 s showing the ROIs at the inner limiter where the analysis was performed. In the same way, **figures 4.18 a) and b)** show a zoom of the mean frames again over 100 ms of the interaction region at t = 47.6 s when the plasma was leaning at the outer limiters. The average intensities <I> in counts (c) over the marked ROIs are written on the images. The corresponding estimated camera radiances using the calibration factors and the obtained Y_{Be}^{eff} at the inner and outer limiters using **equation (3.4)** are listed in **table 4.1**.

	IN Spectro	IN Camera	OUT Camera
L_{BeII} (ph s^{-1} cm^{-2} sr^{-1})	4.5×10^{13}	6.6×10^{13}	6.8×10^{13}
L_{H_α} (ph s^{-1} cm^{-2} sr^{-1})	1.0×10^{15} ($L_{H_\alpha} \approx 30\ L_{H_\gamma}$)	1.3×10^{15}	1.8×10^{15}
Y^{eff}_{Be}	0.08	0.09	0.07

Table 4.1: Radiances L and effective sputtering yields Y^{eff}_{Be} measured with the cameras.

Comparing the spectroscopy data with those of the cameras when the plasma is leaning at the inner limiters, we see that the radiances estimated with the cameras are about 30% higher. Apart from the calibration errors, it is to be expected that the camera radiances are higher because the analysed light comes from the region with strongest interaction around the strike point of the plasma at the limiter whereas those of the spectroscopy system come from a limiter border at the SOL region in the shadow of the limiter corner. Concerning the measured Y_{Be}^{eff}, similar values are obtained with both system.

Looking to the camera radiances at the outer and inner limiter configurations, we observe similar values for the BeII line and somewhat larger values at the outer limiter for the H_α one. Interestingly, the estimated height of the main emission or erosion regions marked by the ROIs, where > 80% of the emission falls in, is of about 90 cm for the outer and 130 cm for the inner limiters. This indicates that the ion flux SOL plasma decay length is shorter when the plasma is leaning at the outer limiters than at the inner ones in agreement with probe measurements [4.2].

Finally, comparing these results with those of **section 4.1** we see that for similar densities ($n_e dl \approx 4.5 \times 10^{19}$ m^{-2} or $\langle n_e \rangle \approx 2 \times 10^{19}$ m^{-3}), the spectroscopy measured L_{H_γ} at

their maxima are similar to those of **figure 4.3a**, about 3.5 x10^{13} ph s^{-1} cm^{-2} sr^{-1}, indicating similar plasma fluxes. However, the measured L_{BeII} of the present example are a factor of about two lower, as also Y_{Be}^{eff}, equal to 0.08 here and was about 0.2 for the D plasma. The same was observed comparing different "Limiter cycling plasmas" in H and D. This is attributed to the isotope effect on the sputtering yield. The plasma here analysed is of H instead of D. The isotope effect on the Be sputtering yields was studied many years ago comparing ion beam experiments and also numerical simulations [4.3]. The result was that H has at least a factor of two lower sputtering yield than D for ion energies of 50 eV – 1 keV. This isotope effect on Y_{Be}^{eff} has been systematically observed recently with both, the spectroscopy system and the cameras during the last H campaign in JET in all kind of limiter plasmas and will be presented next in a separate work together with the data being collected at the moment from the actual T campaign.

5. On-going work

A more ambitious objective would be to extend the here described Be erosion studies using cameras to plasmas with diverted configuration and if possible to high power H-mode plasmas with ELMs in ITER relevant operational scenarios. Previous work including Be erosion modelling during ELMs [5.1] can be resumed and expanded. To explore this possibility and also to show the new arising difficulties, an example of a dithering L-H mode plasma near the density limit with 5 MW NBI and 5 MW of ICRH additional heating power is presented here.

Figure 5.1 shows the magnetic configuration of the analysed diverted plasma and in **figure 5.2** is embedded a video-clip recorded by the cameras. The first part corresponds to a 1 second period taken with the Be II filtered camera with τ_{exp} = 3 ms and 80 fps. The emission comes mainly from the limiters, the divertor and the ICRH antenna at the image background. Than follows a clip of 10 ms duration within the same time interval of the Fast camera looking to the outer wall with τ_{exp} = 50 μs and 2x10^4 fps. The bright emission region above the divertor, where the signal is saturated, corresponds to the D outer mid-plane puffing (see later **figure A.4**) that as expected is not visible with the Be II filtered camera. Just left to it is the outer limiter where the following Be erosion study is focused. Filamentary structures drifting radially out and rotating upwards can be recognized thanks to the fast framing speed. They are shown enhanced in last part of the video by subtracting the background intensity. A separate study of the fast camera observation of these well-known coherent filamentary structures linked to the plasma convective transport towards the walls, finally the main responsible of the plasma-surface interaction, will be presented elsewhere.

The two frames of **figure 5.3** correspond to average images over 3 ms of the upper left region from the Fast camera. The emission from the marked ROI along the upper part of the outer limiter is going to be analysed here in detail. The upper picture with higher intensity corresponds to an L-mode, the lower to an H-mode dither. The weaker emission intensity during the H-mode dither is attributed to lower plasma fluxes due to the better plasma confinement. The time traces for a period of 120 ms of the Fast camera mean intensity within this ROI where the dithers can be clearly distinguished

are plotted in **figure 5.4**. The bottom plot is a zoom of the marked yellowish period. The vertical stripes mark the 3 ms exposure time periods where the average images of **figure 5.3** were integrated, in red for the L- and in blue for the H-mode. The reason of selecting these two time periods will be explained in the next paragraph.

When looking the video-clip of the Be II camera it can be noticed that the flickering emission intensity blinks from one frame to the next. This is because the time between two consecutive frames is of 12.5 ms while the exposure time is 3 ms, meaning that there is a "dead time" of 9.5 ms between frames. Since the H-L periods of the dithers last about 3 to 6 ms the camera sensor is randomly exposed between the upper and lower intensity ranges. In certain frames it will capture light during a whole L- or H-mode period showing approximately its lowest and highest values as the two consecutive frames of **figure 5.5.** The equivalent ROI to the one selected for the Fast camera at the upper part of the outer limiter where the analysis is done is marked on the images. The fluctuating time evolution of the mean Be II emission intensity within this ROI is shown in **figure 5.6**. The red and blue vertical stripes mark the L and H camera periods corresponding to the frames of **figure 5.5** and the horizontal lines their mean emission intensities within the ROI. The selected 3 ms exposure time windows in fact correspond to the same periods of the averaged Fast camera frames of **figure 5.3** and where the respective emission fluxes will be analysed to estimate Y_{Be}^{eff} .

The final step is thus to quantify the information, now complicated by the time-varying intensities as shown before. Here we simply analyse the ROI mean intensity values obtained for the two shown frame pairs where the exposure time matches approximately a L- and H-mode period. The corresponding radiances are calculated with the known calibration factors and the same simplified S/XB method is applied here to obtain Y_{Be}^{eff} . The new uncertainties when applying the method with diverted plasmas will be discussed in the next section. The results are shown in **table 5.1** and following preliminary findings can be outlined. The obtained effective sputtering yields are about one order of magnitude lower than those of the Ohmic limiter plasmas in agreement with published data [5.2]. The main reason of this was attributed to the sensibly lower energy of the impacting ions on to the limiters coming from the SOL in diverted compared to limiter plasmas. An interesting finding is that Y^{eff}_{Be} is about 50% larger during the L- than during the H-mode dithers. This is because for the L-mode the D_α photon fluxes increase by about 35%, whereas those of BeII by a factor of two with respect to the H-mode phase. Compared to the typical fluxes of medium- to high-density Ohmic limiter plasma (**table 4.1**), the estimated D_α photon fluxes at the limiters are sensibly larger, whereas those of Be II are similar or slightly lower.

It must be remembered that these are preliminary conclusions since the applicability of the simplified S/XB method must be re-evaluated for diverted plasmas as will be discussed later. This is because the analysed emission mainly comes from the cooler SOL region in front of the limiters, where a lower $R_{S/XB}$ ratio is to be expected. This would mean that the here given Y_{Be}^{eff} values are most probably overestimated due to this. For example, if we take $\langle T_e \rangle$ = 10 eV and $\langle n_e \rangle$ = 1 x10^{19} m^{-3} as mean parameters

of the up-stream SOL plasma at the limiters, than the $R_{S/XB}$ ratio would be about the half and thereby also the estimated Y_{Be}^{eff} values.

Apart from these general preliminary observations, whose uncertainties will be discussed in the final section, interesting is the appearance of the strong interaction region at the upper inner limiters (see video). The Be II fluxes there are similar or even stronger than at the outer limiters. This is in principle unexpected because they are in the shadow of the outer limiters and their relative distance to the Separatrix is nearly twice (see **figure 5.1**). Poloidal SOL-plasma drifts may be the origin of this interaction, something to be assessed with edge plasma transport codes in the future. Anyway, such kind of observations revels the importance of visualising the whole first wall field using wide-angle view cameras in order to have a complete understanding of the erosion mechanisms.

	L	H
L_{BeII} (ph s^{-1} cm^{-2} sr^{-1})	8.0 x10^{13}	4.0 x10^{13}
L_{D_α} (ph s^{-1} cm^{-2} sr^{-1})	9.2 x10^{15}	7.3 x10^{15}
Y^{eff}_{Be}	0.016	0.01

Table 5.1: Radiances L and effective sputtering yields Y^{eff}_{Be} measured with the cameras at the outer limiters.

6. Summary and discussion

In this work we have explored the capacity to measure the plasma and Be fluxes to estimate Y_{Be}^{eff} from two visible cameras with the same wide-angle view. This allows to make 2-dimensional measurements of the whole vessel including inner and outer limiters and also to obtain the spatial distribution of the main plasma-surface interaction regions, the so-called "wetted areas". A simplified S/XB method was used here for the analysed Ohmic limiter plasmas for which the detailed edge plasma characterisation is unnecessary. To calculate Y_{Be}^{eff} we have taken advantage of the fact that the ratio of the S/XB coefficients of the measured atomic lines that are used to convert the photon to particle fluxes has a relatively small dependence on n_e and T_e for limiter plasmas near the LCFS. When making this approximation we accept an error in the calculation that is estimated to be < +/- 30%. To this error, the uncertainty due to the molecular contribution to the D_α emission as discussed in section 3 must be added.

A large set of Ohmic limiter plasmas have been analysed along the present work and some examples are exposed here. These include cases from "Limiter-erosion" experiments with a density ramp, "Cycling cleaning pulses" and "Limiter start-up"

plasmas that precede all JET discharges. The estimated Y_{Be}^{eff} values here obtained are generally in good agreement with previous work. The camera measurements were also validated for the same plasmas with those obtained with the spectroscopy system that looks to a discrete point at the inner limiter. For $<n_e>$ = 1.5 – 3.5 x10^{19} m^{-3}, the measured yield range was of 0.07 $< Y_{Be}^{eff} <$ 0.3. It increases at lower densities and can run-out to values > 1, something attributed to enhanced Be self-sputtering [11, 12]. In this critical operation regime for each impinging plasma ion, one or more Be atoms are sputtered from the surface. In accordance with prior studies, the yield generally decreases with increasing average plasma density $<n_e>$. However, this may not hold if the measurement is not made at the strike point location of the plasma at the limiter (the region of maximum interaction).

Additionally, along the present study following observations have been made:

- The local emission coming from the discrete small area where the spectroscopy system is looking at is sensible to the exact spatial plasma-surface interaction distribution where different fluxes and local plasma parameters may change. This fact should be taken into account when interpreting the spectroscopy data and attention should be paid when linking its measurements to the real erosion field at the limiters and also to global plasma parameters as $<n_e>$. The use of cameras instead gives a global view of the erosion field.

- Comparing H and D plasmas, an isotope effect on Y_{Be}^{eff} has been observed: the erosion yield for H plasmas is typically the half then for D. This will be shown in more detail in a separate publication together with on-going measurements in T plasmas.

- Analysing “Limiter cycling pulses” in plasma configurations with same densities, the measured Y_{Be}^{eff} is similar at the inner and outer limiters. However, the wetted area is larger at the inner limiters and thereby the overall integrated plasma and Be fluxes.

- A diverted plasma with additional heating and in a dithering L-H confinement mode has been preliminarily analysed using the same method. Although further work is necessary to clarify new uncertainties as will be discussed in the next paragraph, lower values of Y_{Be}^{eff} by at least an order of magnitude were estimated in agreement with previous studies [5.2]. As will be discussed, these results are only preliminary due to larger uncertainties. Interestingly, thanks to the wide-angle view of the cameras, strong Be fluxes at the upper part of the inner limiters where observed, something in principle unexpected since there the surface was in the shadow of the outer limiters and far from the Separatrix. The same has been seen for other L- and H-mode plasmas and will be the subject of next studies.

Concerning future work and especially if diverted plasmas are going to be analysed, following important points will be further addressed:

- The simplified S/XB method must be re-evaluated since the D_α and Be II atomic emission is expected to come in diverted plasmas from SOL plasma regions where the upstream T_e is expected to be smaller than for limiter plasmas (< 25 eV).

Therefore, in order to assess the S/XB coefficients, the upstream radial n_e-, T_e- along the emission profiles must be estimated. As proposed in [6.1] when modelling the JET upstream SOL plasma for the impurity transport code ERO and where the general lack of this information is a main uncertainty source, n_e could be measured with the Li-beam diagnostic and T_e by extrapolating Langmuir probe data to plasma edge measurements near the Separatrix with Thomson scattering. The best would be to use the experimental n_e and T_e profiles to simulate the D and Be emission profiles with EDGE2D-EIRENE and use the camera images to validate the simulated emission distribution in the vessel thereby closing the loop. Unfortunately, this must be repeated for each plasma type with its characteristic radial SOL profiles and this will suppose a very large effort.

- In diverted plasmas the D_α-emission at the divertor is up to two orders of magnitude larger than at the limiters and light reflection at the limiter surfaces may contaminate the emission measurements. Fortunately this is not the case for the BeII emission, which is typically of the same order at limiters and divertor. To discriminate light reflections, sometimes the comparison of the emission intensity time traces at the divertor and limiters in time varying conditions such as ELMs can be used to estimate the contribution of reflections. Also, the characteristic spatial emission pattern of the filamentary structures as seen in L- and H-mode during ELMs can help to discard reflected light, since its contribution is expected to be uniform and not with a characteristic pattern. The best to assess this problem however would be to simulate the divertor emission and use ray-tracing methods to get synthetic images and compare them with real camera images (see e.g. [6.2]). This again will suppose a large effort, since the reflection patterns will change the different plasmas.

7. References

[0] Matthews G.F. et al 2013 J. Nucl. Mater. 438 S2
https://doi.org/10.1016/j.jnucmat.2013.01.282
[1] S Carpentier et al 2011 J. Nucl. Mater. 415 S165
https://doi.org/10.1016/j.jnucmat.2010.10.081
[2] D Borodin et al 2011 Phys. Scr. T145 14008
https://doi.org/10.1088/0031-8949/2011/T145/014008
[3] D Borodin et al 2019 Nucl. Mat. and Energy 19 510
https://doi.org/10.1016/j.nme.2019.03.016
[4] A Kirschner et al 2015 J. Nucl. Mat. 463 116
https://doi.org/10.1016/j.jnucmat.2014.10.072
[5] J Romazanov et al 2021 Nucl. Mat. and Energy 26 100904
https://doi.org/10.1016/j.nme.2021.100904
[6] K Schmid et al 2015 J. Nucl. Mat. 463 66
https://doi.org/10.1016/j.jnucmat.2014.11.109
[7] A Khan et al Nuclear Materials and Energy 20 (2019) 1006742
https://doi.org/10.1016/j.nme.2019.100674
[8] N Den Harder 2016 Nucl. Fusion 56 026014
https://doi.org/10.1088/0029-5515/56/2/026014
[9] A Kirschner et al 2019 Nucl. Mat. and Energy 18 239
https://doi.org/10.1016/j.nme.2019.01.004
[10] A Huber et al 2019 Nucl. Mat. and Energy 18 118
https://doi.org/10.1016/j.nme.2018.12.009

[11] M Stamp et al 2010 J. Nucl. Mat. 415 S170
https://doi.org/10.1016/j.jnucmat.2010.12.038
[12] S Brezinsek et al 2014 Nucl. Fusion 54 103001
https://doi.org/10.1088/0029-5515/54/10/103001
[13] S Brezinsek et al 2015 Nucl. Fusion 55 063021
https://doi.org/10.1088/0029-5515/55/6/063021
[14] A Widdowson et al 2014 Phys. Scr. T 159 014010
https://doi.org/10.1088/0031-8949/2014/T159/014010
[15] D Borodin et 2014 Phys. Scr. T 159 014057
https://doi.org/10.1088/0031-8949/2014/T159/014057
[16] J Romazanov et al 2019 Nucl. Mat. and Energy 18 331
https://doi.org/10.1016/j.nme.2019.01.015
[17] S Salasca et al 2015 Fusion Eng. Des. 96–97 932
https://doi.org/10.1016/j.fusengdes.2015.02.062
[18] R Reichle et al 2012 Rev. Sci. Inst. **83** 10E520
https://doi.org/10.1063/1.4734487
[19] M Medrano et al 2021 Fus. Eng. Des. 168 112651
https://doi.org/10.1016/j.fusengdes.2021.112651
[20] C Pastor et al 2021 Fus. Eng. Des. 168 112607
https://doi.org/10.1016/j.fusengdes.2021.112607
[21] A Huber et al 2019 Nucl. Mat. and Energy 18 118
[22] J Karhunen et al 2020 Nucl. Mat. and Energy 25 100831
[23] U losada et al 2020 Nucl. Mat. and Energy 25 100837

[2.1] M Clever *et al 2013* Fusion Eng. Des. **88** 1342
[2.2] V Huber *et al 2019* Nucl. Fusion **59** 076016
[2.3] E de la Cal et al 2020 Plasma Phys. Control. Fusion 62 035006
https://iopscience.iop.org/article/10.1088/1361-6587/ab5fb1
[2.4] V Huber *et al* 2017 Fusion Eng. Des. **123** 979

[3.1] K H Behringer et al, PPCF 31 (1989) 2059
[3.2] ADAS, http://adas.phys.strath.ac.uk
[3.3] Ph Mertens et al 2001 Plasma Phys. Control. Fusion 43 A349
[3.4] S Brezinsek et al 2005 Plasma Phys. Control. Fusion **47** 615
[3.5] E de la Cal et al 2008 Nucl. Fusion 48 095005
[3.6] The JET Team 1989 J. Nucl. Mat. 162-164 3
[3.7] S Clement et al 1990 J. Nucl. Mat. 176-177 432
[4.1] D Borodin et al 2016 Nucl. Mat. and Energy 9 604
https://doi.org/10.1016/j.nme.2016.08.013
[4.2] C Silva et al 2014 Nucl. Fusion 54 083022
https://doi.org/10.1088/0029-5515/54/8/083022
[4.3] J Roth et al 1997 Fus. Eng. Des. 37 465
https://doi.org/10.1016/S0920-3796(97)00091-4
[5.1] I Borodkina et al 2016 Contrib. Plasma Phys. 56 201610032
https://doi.org/10.1002/ctpp.201610032
[5.2] S Brezinsek et al 2015 Nucl. Fusion 55 063021
[6.1] J Romazanov et al 2019 Nucl. Mat. and Energy 18 331
[6.2] M Carr et al 2019 Rev. Sci. Instrum. 90, 043504
https://doi.org/10.1063/1.5092781

Appendix: Camera calibrations

The cameras have been cross-calibrated against the absolute radiance measurements of the divertor spectroscopy system that collects light from discrete chords looking from an upper port to the upper inner divertor corner (see section 2). For the unfiltered camera also a calibration has been done by measuring its response to a D_2 puffing with known gas flow rate, so as to relate camera signal to D flux density. For the calibrations it has been assumed that the plasma emission layer is a thin planar radiation source that radiates isotropically light far from the detector. A picture of the cameras view is shown in **figure A.1** where the here monitored outer limiter 4B and inner limiter 4Z are marked and also the upper inner divertor region observed for the calibrations (T0 and T1 correspond to divertor Tiles 0 and 1 in JET nomenclature). The corresponding approximate angles α between the cameras lines of view and the surface normals are also displayed. The radiance L is the radiant emitted photon flux by a given surface per unit solid angle per unit projected area on the surface. The equation used here to relate the camera signal rate I'(counts/s) to L (ph s^{-1} cm^{-2} sr^{-1}) through the calibration factor c is:

(A.1) $L = c\ I'\ (\cos \alpha)$,

where the term $(\cos \alpha)$ corrects for the geometrical effect as shown in **figure A.2**. This accounts for the larger real area imaged onto a pixel at oblique viewing angles. The shallower the viewing angle α is, the larger the camera intensity for same radiance as can be seen in **figure A.6**. This "geometrical effect" has only influence in the estimation of the absolute fluxes, not on the sputtering yield, since the term $(\cos \alpha)$ vanishes when calculating the quotient of the D_α- and Be II-radiances having the same view. Although when estimating calibration factors large errors must be generally, it has confirmed along the present work that the so estimated camera radiances were consistent with measurements of the spectroscopy system at the inner limiter (see section 4.2.3).

A.1 Calibration of visible Fast camera to measure D_α-fluxes

The plasma emission measured by the unfiltered Fast camera is clearly dominated by the strong D_α-line. This was firstly checked comparing its data with the ones obtained with the spectroscopy camera with same view but using a D_α- instead of the Be II-line filter. The relative intensities of the video images of both cameras showed very similar values at all viewing regions, including the emission coming from the D gas puffing at the plasma outer mid-plane, later used for calibration issues. The same was done in the past with the other Fast camera in JET comparing similar plasmas with and without D_α-line filtering and using the cross-correlation technique with the D_α-signals of the divertor spectroscopy system [2.3]. This high correlation was also systematically observed during dynamic events such as ELMs with the here used unfiltered camera.

In order to calibrate the Fast camera intensity to obtain absolute D-atom or D_α-photon fluxes, firstly the measured emission intensity coming from a D gas puffing system at the plasma outer mid-plane was analysed. **Figure A.3** left shows the wide-angle view of the Fast camera where this light region from the mid-plane D puffing is marked. The Region of Interest (ROI) selected in the enlarged image to the right corresponds to the region where most emission from the injected D comes from. Making a dimensional conversion of pixels to space in the corresponding image plane this imaged area was estimated to correspond to $A' \approx 1800$ cm^2. To get the real area A of the emission region, A´ has to be to multiplied by $(\cos \alpha)^{-1}$, where $\alpha \approx 55^o$ is the angle between the observation line of view and the emission surface normal (**figure A.4**) so that $A \approx 3200$ cm^2. The D constant puffing rate F_D from this calibrated valve was for this plasma period equal to 6.6 x10^{21} D s^{-1} that divided by the estimated emission area gives a mean flux density $\Phi_D \approx 2.1$ x10^{18} D s^{-1} cm^{-2}. On the other hand, the measured average camera signal intensity of the ROI is I ≈ 2300 counts subtracting the background (about 100 counts) that corresponds to a intensity rate of approximately I´ ≈ 3.4 x10^7 counts/s (exposure time τ_{exp} = 6.7x10^{-5} s). With this, we obtain a calibration factor $k_D \approx 6\,x10^{10}$ that converts the camera signal intensity rate in (count s^{-1}) to D flux density Φ_D in (D s^{-1} cm^{-2}). It should be noted that, as explained in section 3, the number of photons emitted per D atom entering the plasma. i.e. the effective S/XB coefficient, is dependent on n_e and T_e profiles along the emission layer (see **figure 3.1**). Therefore, the calibration factor will depend on the edge plasma parameters in a similar way as $S/XB_{D\alpha}$. Interestingly, the here described method has been repeated for a large number of different plasmas with different magnetic configurations, densities and heating power and the obtained calibration factor differences were less than +/- 20%. Also modifying slightly the ROI dimensions, i.e. making the area somewhat larger or smaller, doesn't affect sensibly the results, since the mean intensity than inversely decreases or increases respectively.

The second proposed method and the one used for the present study is to directly cross-calibrate the camera intensity against the absolute divertor spectroscopy D_α-measurements of discrete chords directed from an upper port to the upper inner divertor corner (see **figure A.5** the chords labelled as DAI1 and DAI4). This has been done for several plasmas and here are shown two examples. The first one is an L-mode plasma with the inner strike point raised at the upper divertor region as displayed in **figure A.5** (JPN #98552). For this plasma the spectroscopy camera, used in the present work for the Be II measurements, was set with a D_β filter. **Figure A.6a** shows a frame of this camera (τ_{exp} = 3 ms) and **Figure A.6b** of the unfiltered Fast camera (τ_{exp} = 1.25 ms) at the same instant during this discharge. The mesh superposed on the upper picture shows the detailed positioning of the divertor tiles that are labelled as in **figure A.5**. The intensity patterns of both images are very similar because the D_β-emission must be very similar to the D_α one, although much weaker. As expected, the divertor spectroscopy array signals show for this plasma time period that most of the D_α-emission came form the upper inner divertor region, more precisely, from the four innermost chords (marked in **figure A.5** are the extremes**).** The mean D_α-radiance of them was during this period

$L_{D_\alpha} \approx 5$ x10^{15} ph s^{-1} cm^{-2} sr^{-1}. On the other hand, the mean intensity $<I>$ of the unfiltered visible camera in the marked ROI that comprises the main emission region was of 3.5 x10^4 counts, corresponding to a mean intensity rate $<I'> \approx 2.8$ x10^7 counts/s. On the other side, for the here analysed ROI the angle $\alpha \approx 45^o$. Thus the calibration factor c_{D_α} to convert the Fast camera intensity rate I' to D_α-radiance L_{D_α} can be estimated using **equation A.1** and is equal to $c_{D_\alpha} \approx 2.5$ x10^8 ph counts^{-1} cm^{-2} sr^{-1}.

The second example is from a NBI heated plasma in a H-L dithering phase showing strong emission oscillations at the observing region. In **figure A.7** is embedded a video-clip of the Fast camera (τ_{exp} = 2 x10^{-5} s) with the ROIs marking the two analysed spots where the spectroscopy chords are looking at and where one of these oscillations can be seen. **Figure A.8** shows in the upper frame the radiance time evolution during 5 wavering of the two D_α-channels and the lower frame the mean intensity of the corresponding ROIs of the camera videos. Again, the high correlations of the signals are clearly visible. The measured D_α-radiance L_{D_α} at the maxima of the last 4 regular oscillations is 1.1 x10^{17} ph s^{-1} cm^{-2} sr^{-1} for channel 3 where the emission maximum is localised. The respective camera intensity at the maximum at ROI 3 is approximately equal to 2 x10^4 counts, corresponding to an intensity rate I′= 1 x10^9 counts/s. Using **equation A.1** and correcting for the estimated camera viewing angle $\alpha \approx 60^o$ we finally get here a calibration factor $c_{D_\alpha} \approx 2.2$ x10^9 ph counts^{-1} cm^{-2} sr^{-1}.

This cross-calibration has been done for other plasmas and c_{D_α} values in the same range were obtained. The final calibration factor which will be used in the present work to convert the camera intensity rate I′ to D_α-radiance L_{D_α} is $c_{D_\alpha} \approx 2.4$ x10^8 ph counts^{-1} cm^{-2} sr^{-1}. The (cos α) correction factor is applied with $\alpha \approx 50^o$ for the observed inner limiter and $\alpha \approx 65^o$ for the outer one.

A.2 Calibration of Be II camera

The Be II filtered camera has been also cross-calibrated by comparing its signal intensity rate with the Be II measurements of the divertor spectroscopy system in a similar way as in the previous section. **Figure A.9** shows a divertor picture as viewed by the cameras where the inner divertor spectroscopy chords 1 and 3 are schematically drawn. A plasma was analysed at the moment when changing from a limiter magnetic configuration to a diverted one. The video-clip of this time period from the BeII filtered camera is embedded in **figure A.10** where the mesh shows the detailed positions of the divertor tiles. The marked regions 1 and 3 at the upper inner divertor correspond to those seen by the spectroscopy channels 1 and 3. **Figure A.11** shows for this time period in the upper frame the measured radiances L_{BeII} of spectroscopy channels 1 and 3, and in the lower one the signals of the camera at the marked corresponding ROIs. As can be seen, there is a very good correlation between their relative intensities. To make the cross-calibration we compare the signals corresponding to channel 3 because of the higher intensity taking a mean value of two selected time instants (see figures). The camera mean-intensity of the ROI number 3 subtracting the offset (300 counts) is $<I> \approx$ 3100 counts or an intensity rate of $<I'> \approx 5.2$ x10^5 counts/s (τ_{exp} = 6 ms). On the other hand, the mean radiance at both instants measured by spectroscopy channel 3 is $L_{BeII} \approx$

5.2 x10^{13} ph s^{-1} cm^{-2} sr^{-1}. Using **equation A.1** and correcting for the estimated camera viewing angle $\alpha \approx 45^{o}$ we finally get here a calibration factor $c_{BeII} \approx 1.4$ x10^{8} ph $counts^{-1}$ cm^{-2} sr^{-1}. This cross-calibration procedure has been done for other plasmas and similar values were obtained. We finally fix a mean of the different estimated values obtaining of $c_{BeII} \approx 1.2$ x10^{8} ph $counts^{-1}$ cm^{-2} sr^{-1}.

Additionally, this camera has an on-chip electron-multiplying sensor and corrections were made to account for the gain settings. For the here analysed plasmas the camera was operated only with small gain variations of only +/- 20%.

Figure 2.1

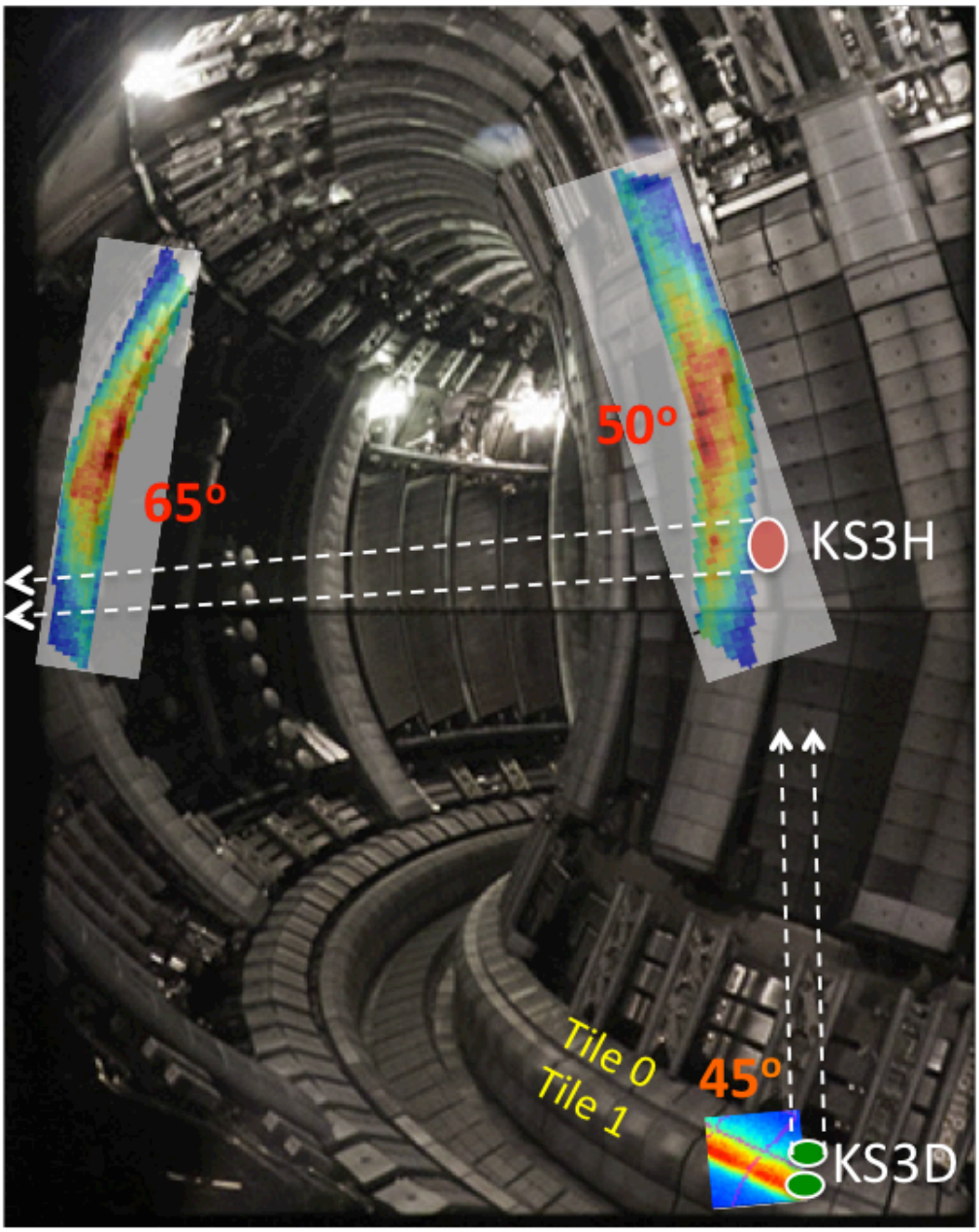

Figure 3.1 a

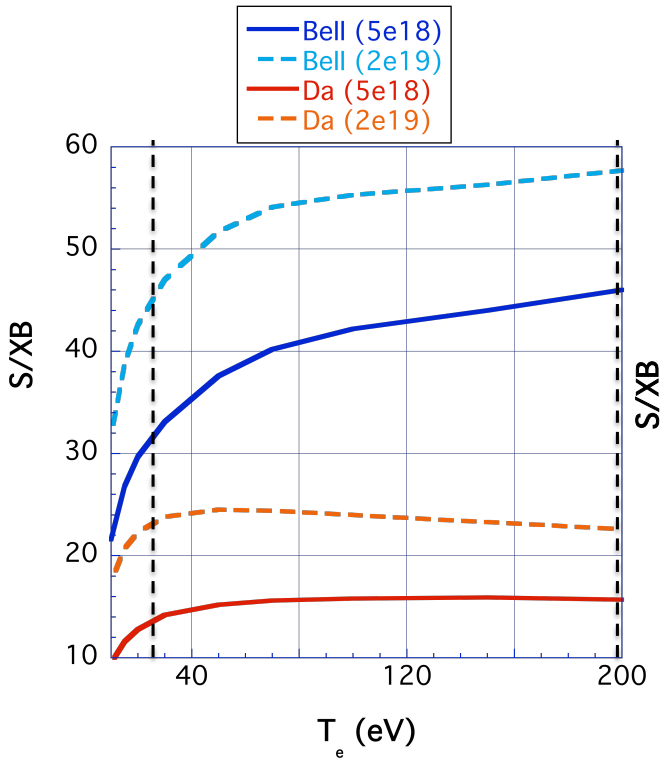

Figure 3.1 b

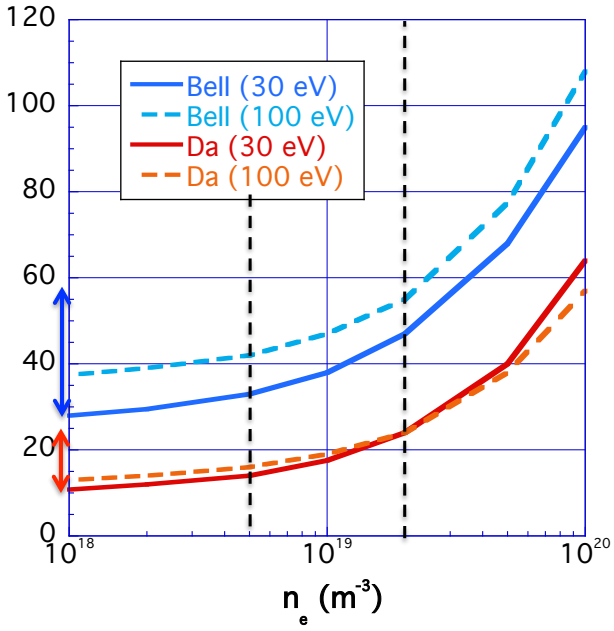

Figure 3.2 a

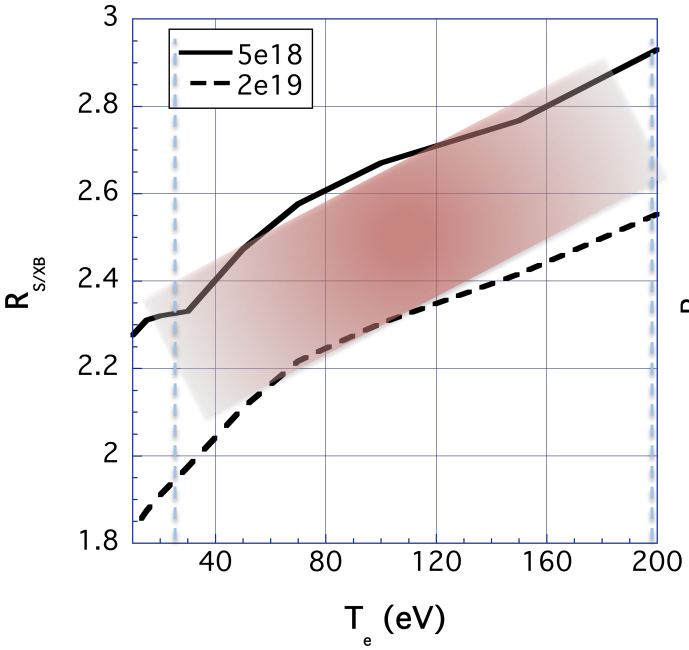

Figure 3.2 b

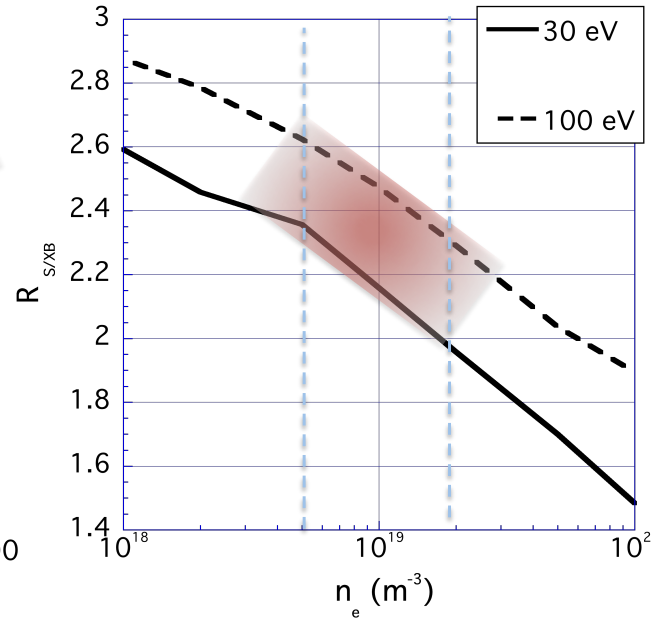

Figure 4.1

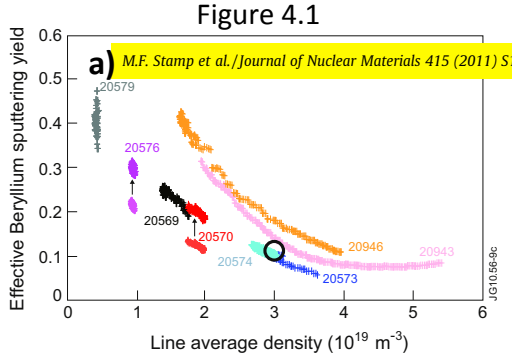

[Ref. 11]

Fig. 3. Limiter beryllium sputtering yield vs. line average density. The black circle at 3.0e19 m^{-3} is the data point calculated using D-gamma rather than D-alpha (see text). For #20570 and #20576, the data using the old S/XB is also shown.

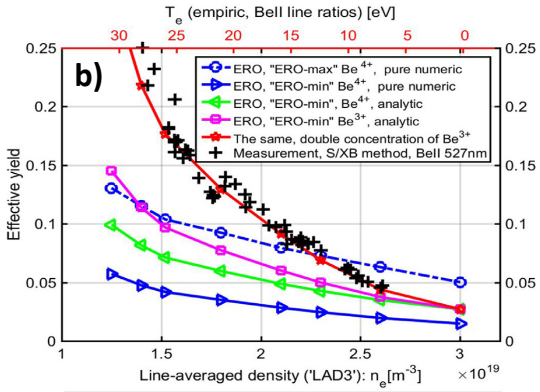

D. Borodin et al./Nuclear Materials and Energy 9 (2016) 604–609 **[Ref. 12 and 5.1]**

Figure 4.2

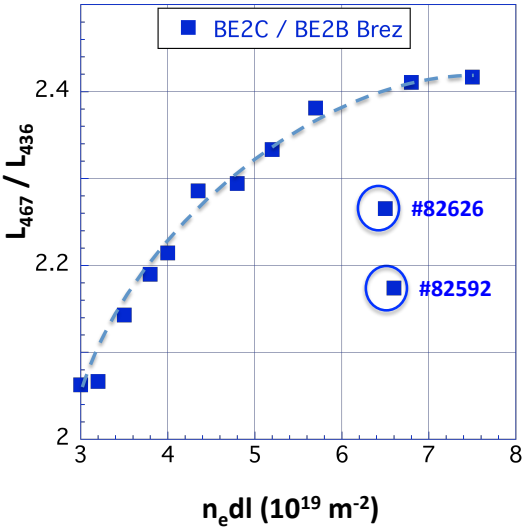

Figure 4.3 a

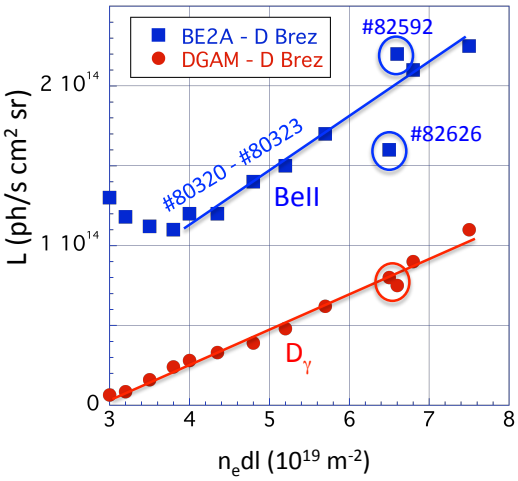

Figure 4.3b

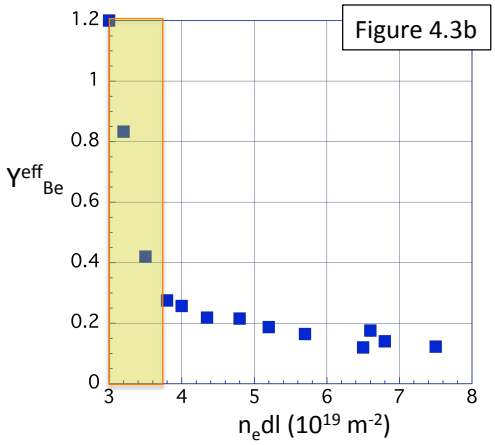

Figure 4.3c

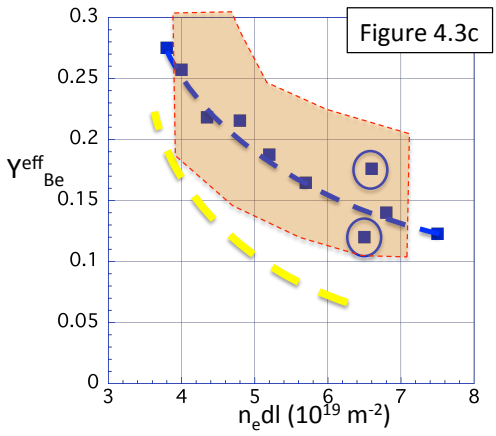

Figure 4.4

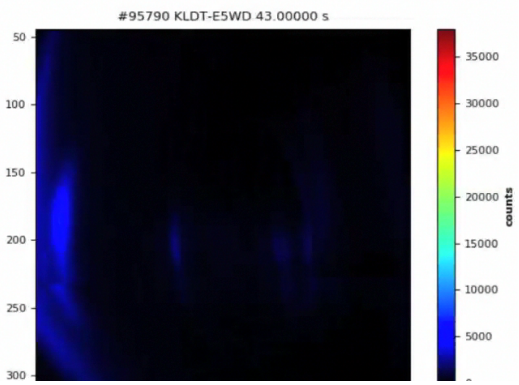

Figure 4.5

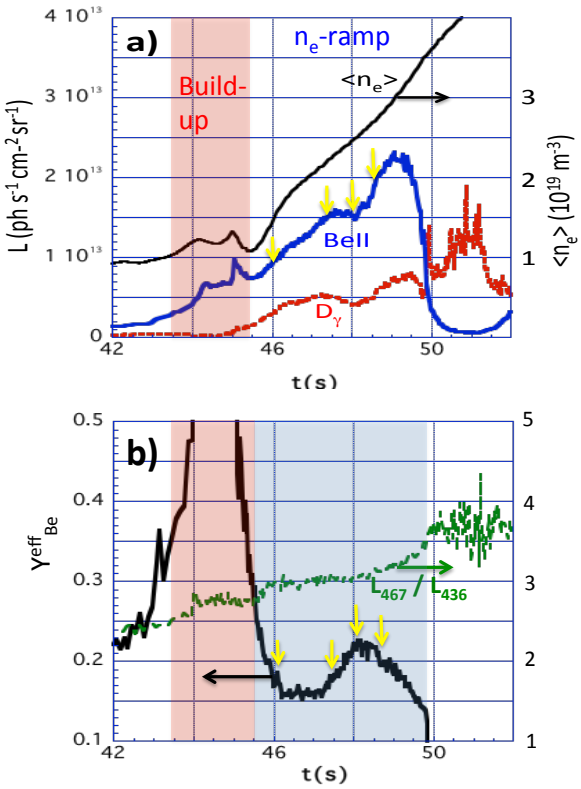

Figure 4.6

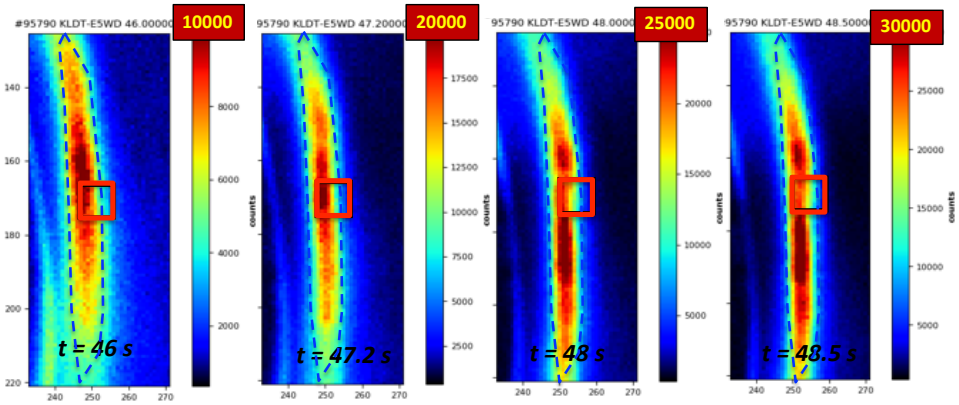

Figure 4.7

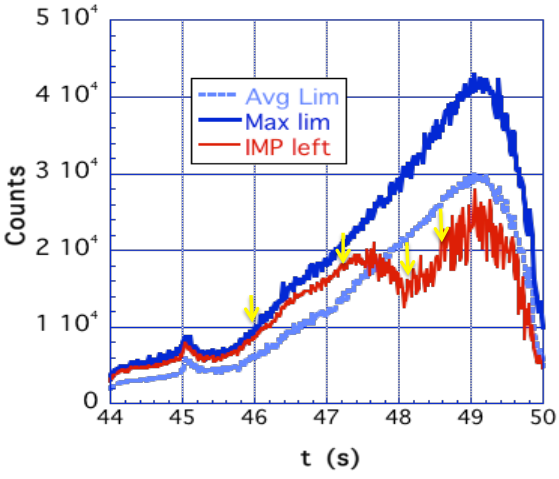

Figure 4.8

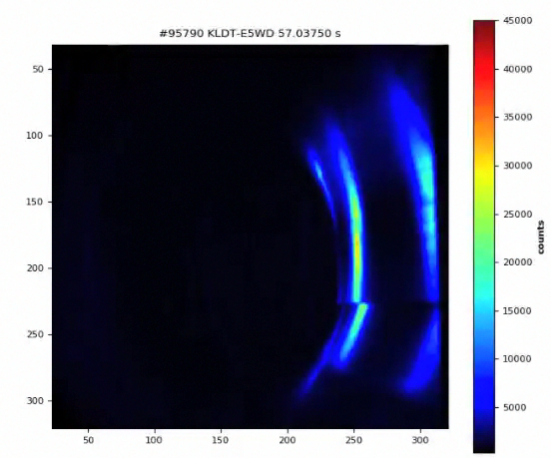

Figure 4.9

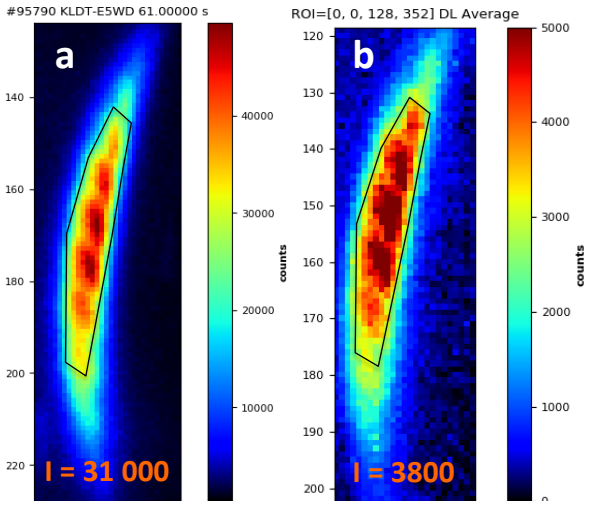

Figure 4.10

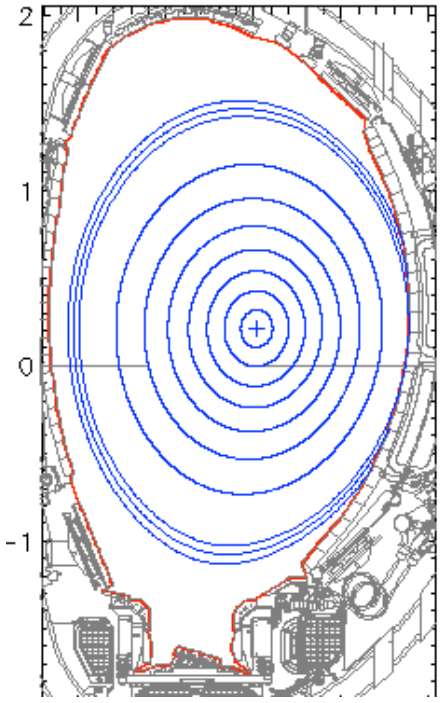

Figure 4.11

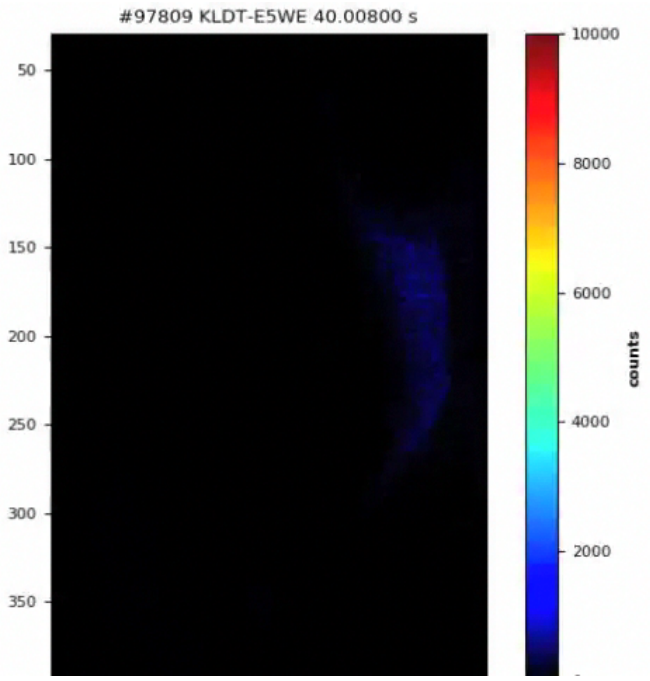

Figure 4.12a

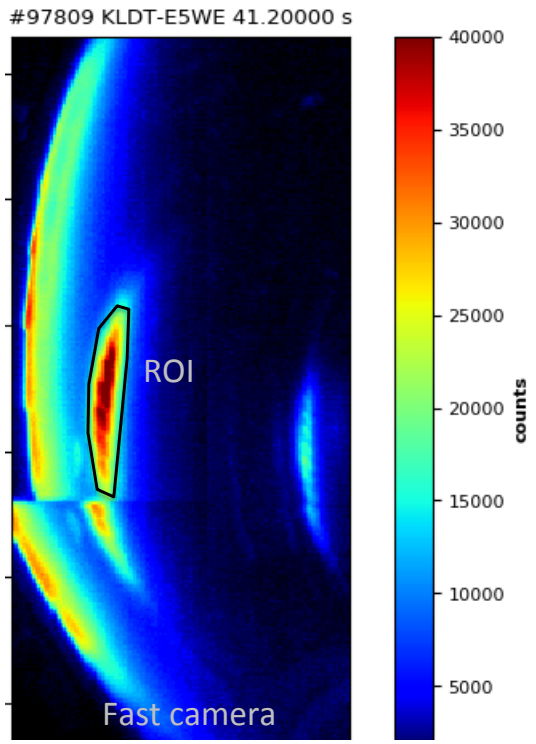

Figure 4.12b

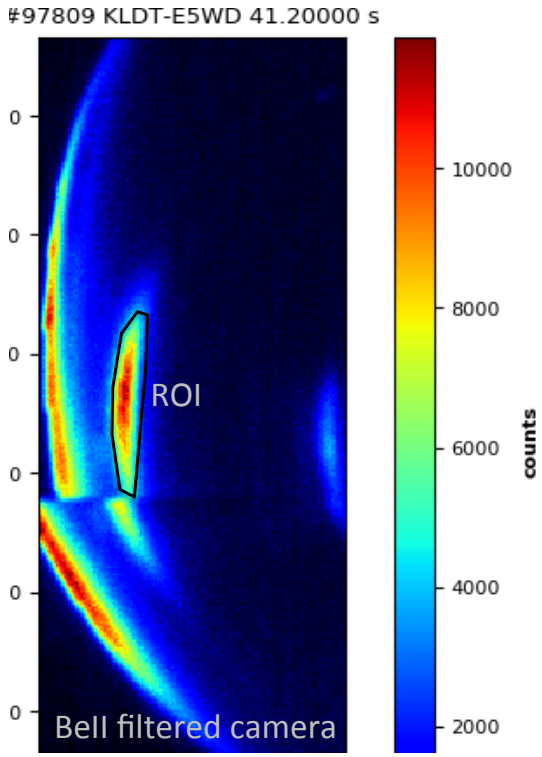

Figure 4.13

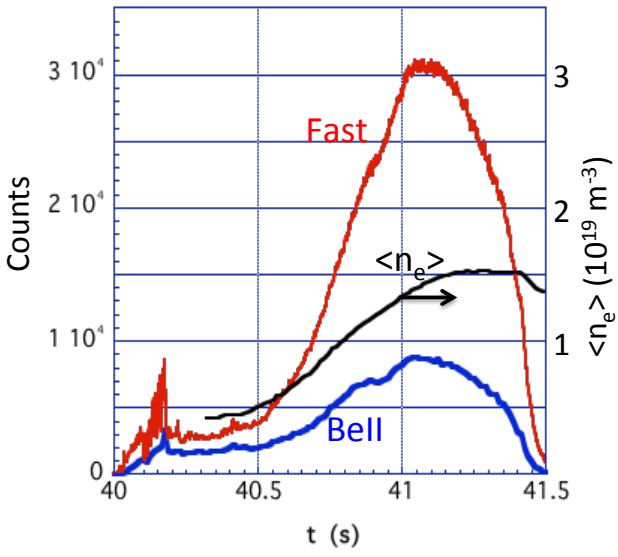

Figure 4.14

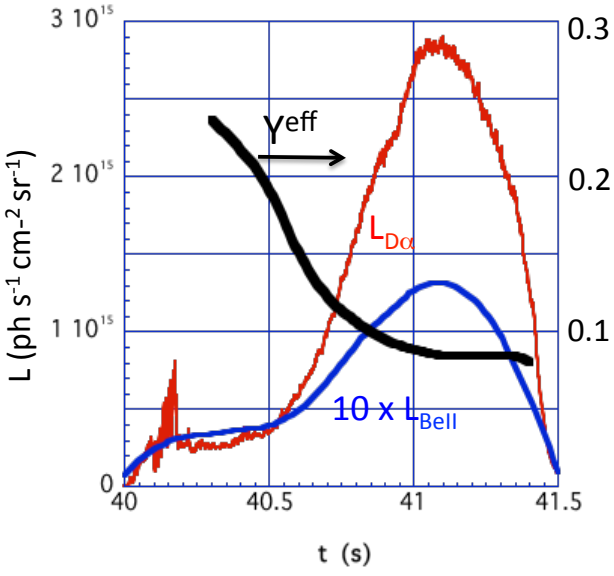

Figure 4.15

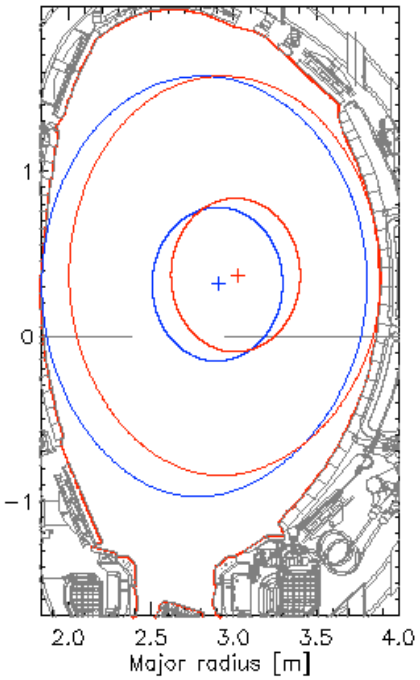

Figure 4.16

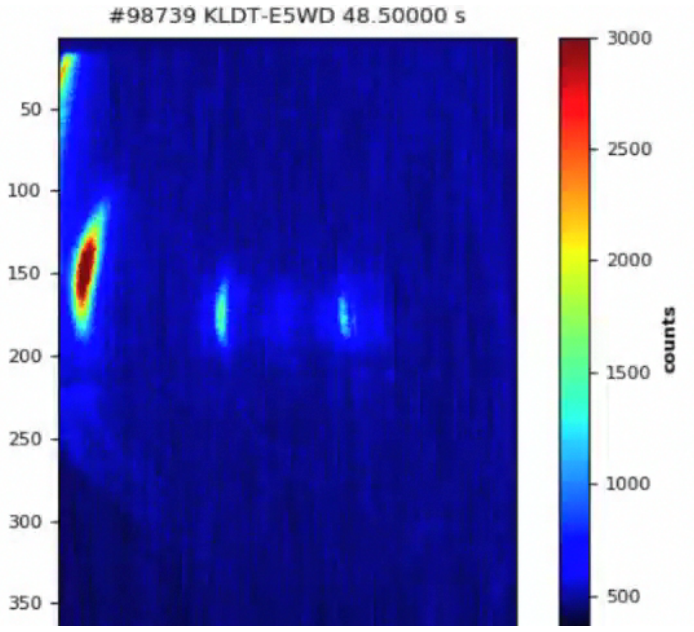

Figure 4.17

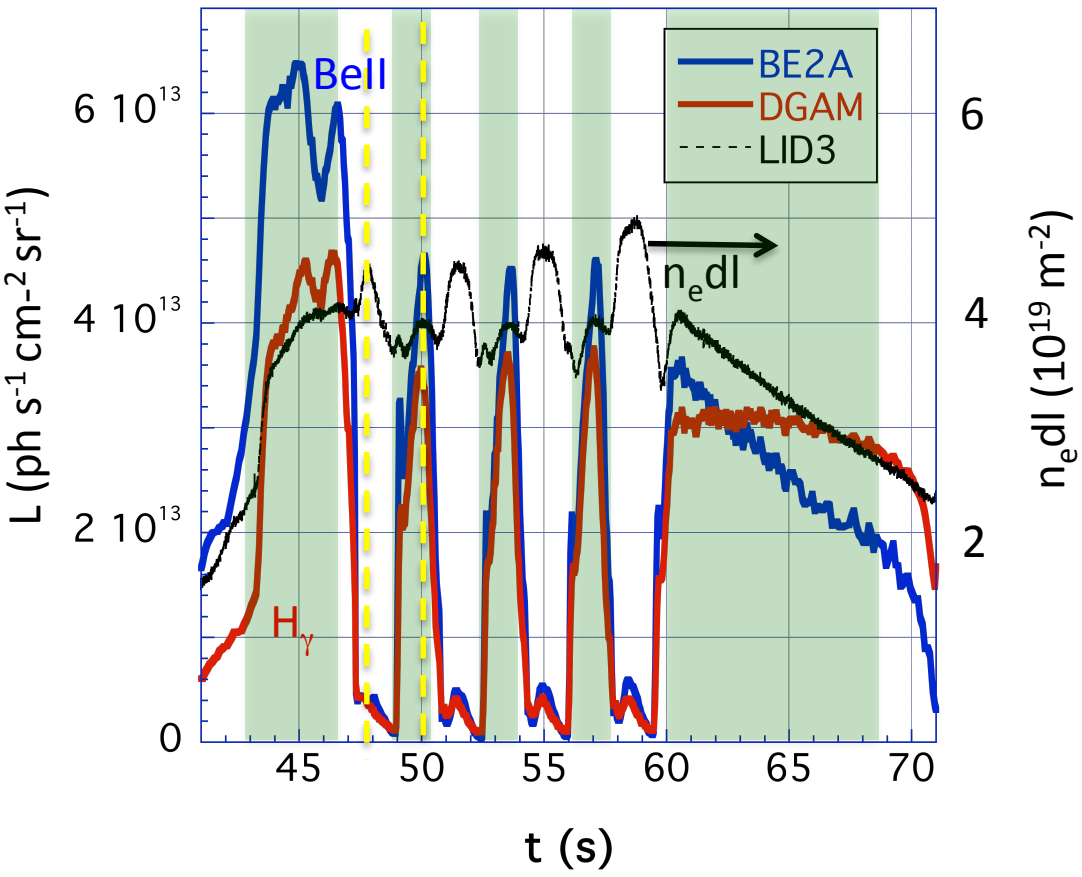

Figure 4.18a

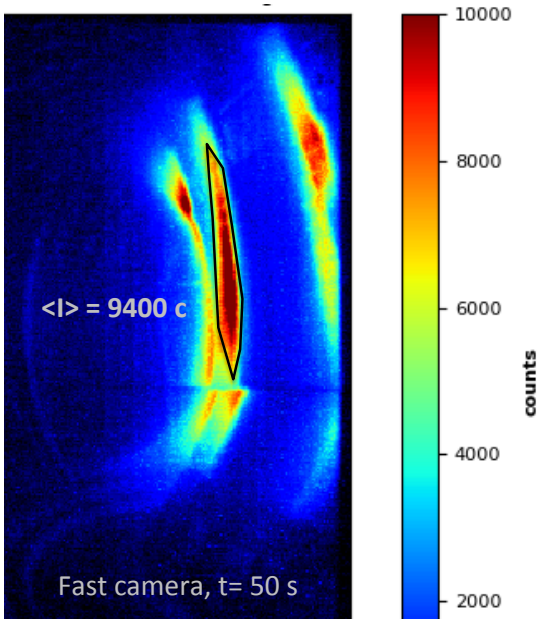

Figure 4.18b

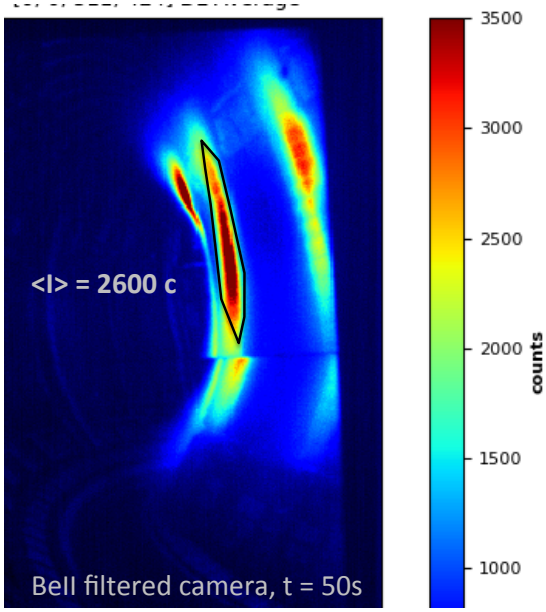

Figure 4.19a

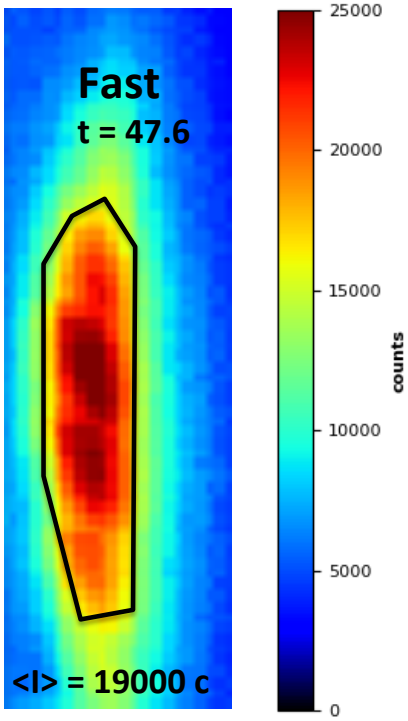

Figure 4.19b

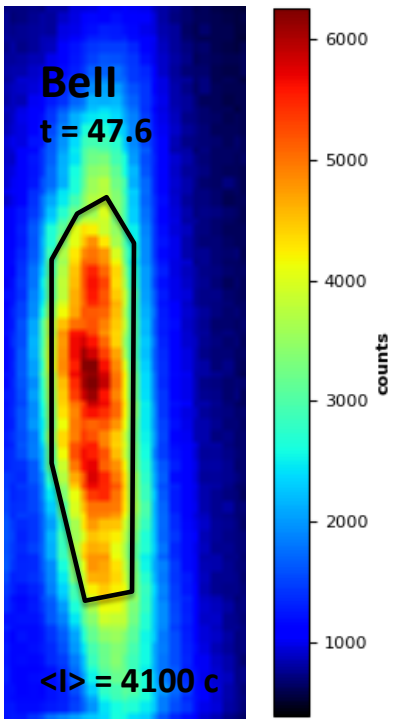

Figure 5.1

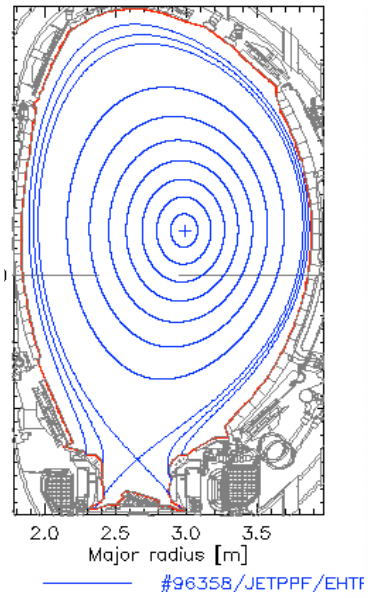

Figure 5.2

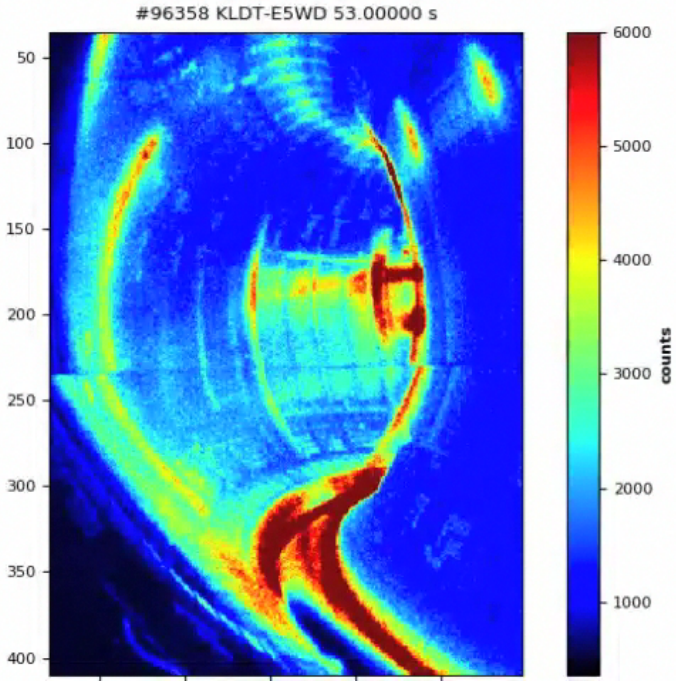

Figure 5.3

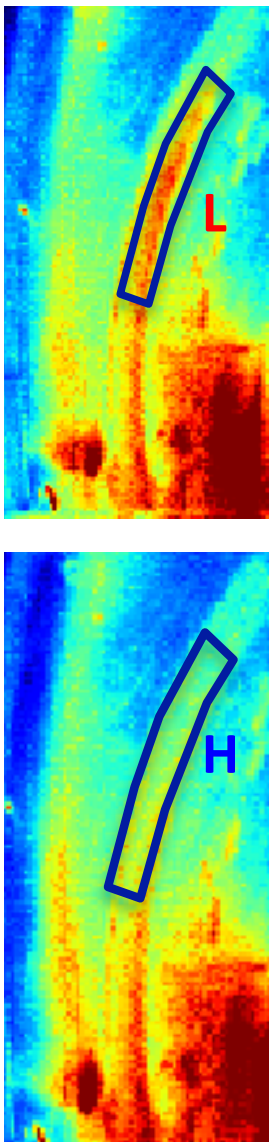

Figure 5.4

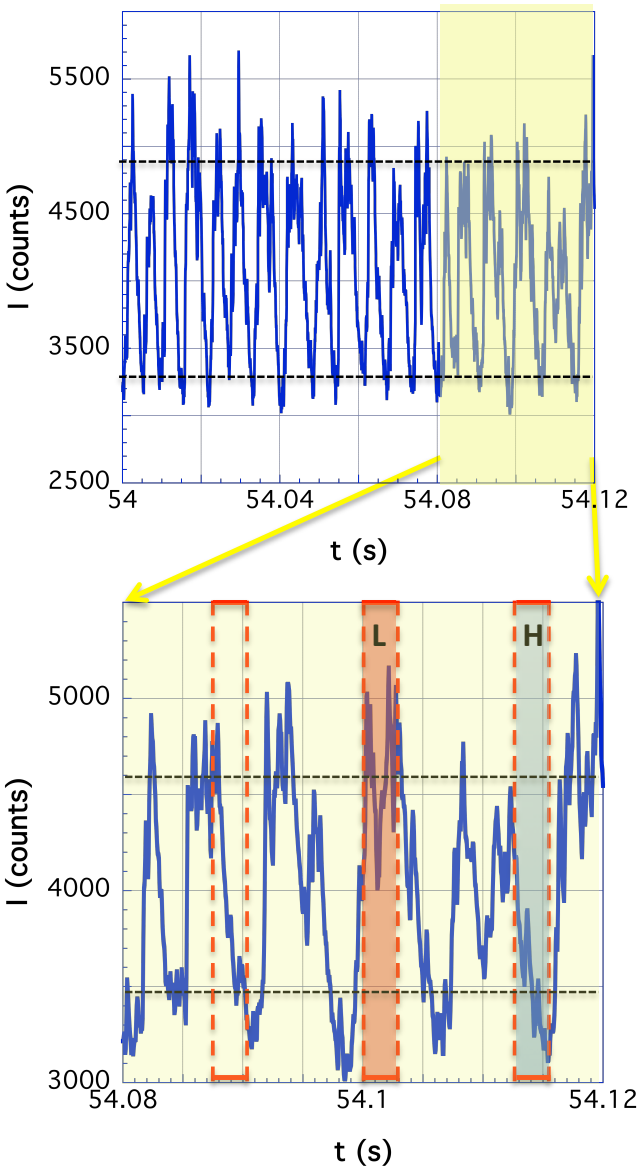

Figure 5.5

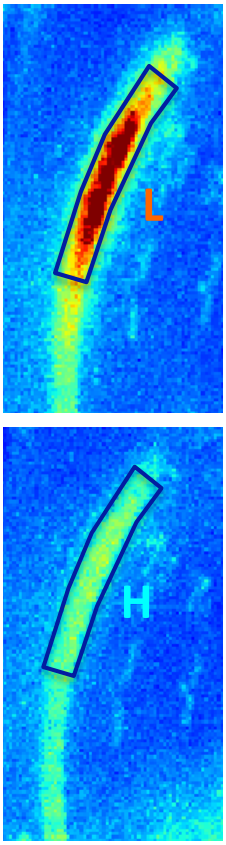

Figure 5.6

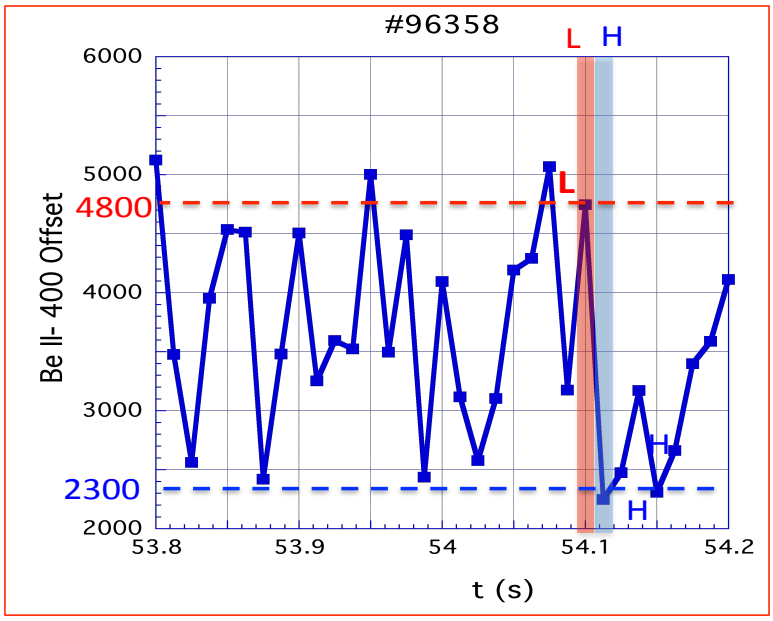

Figure A.1

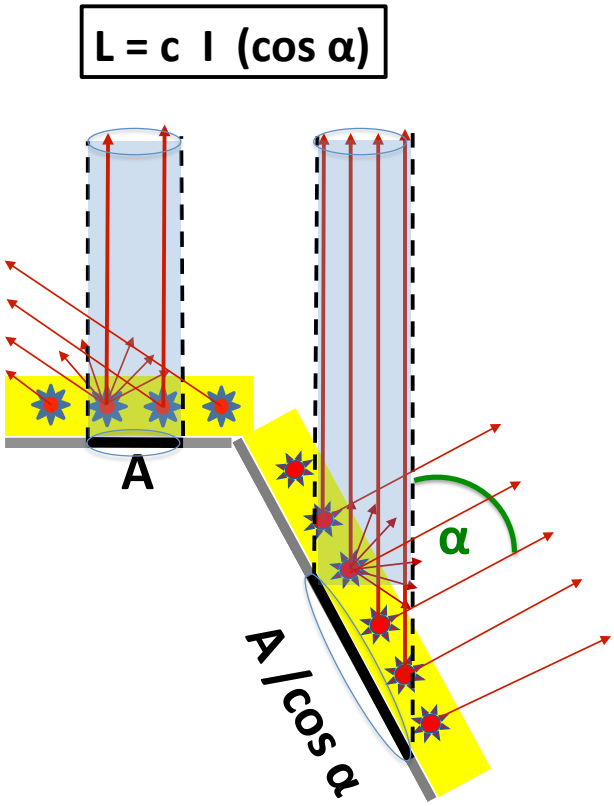

Figure A.3

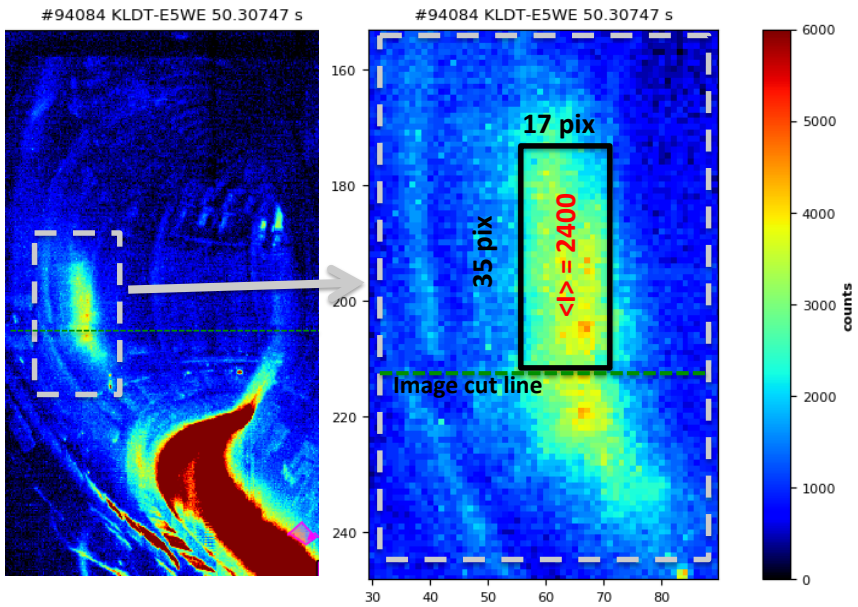

Figure A.4

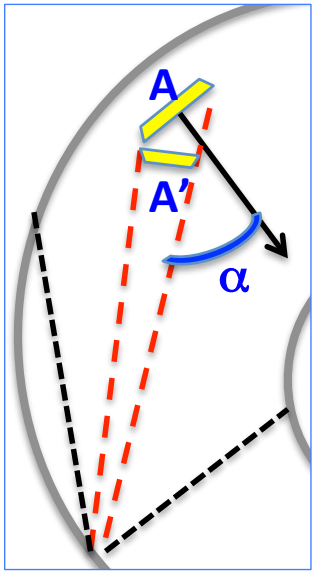

Figure A.5

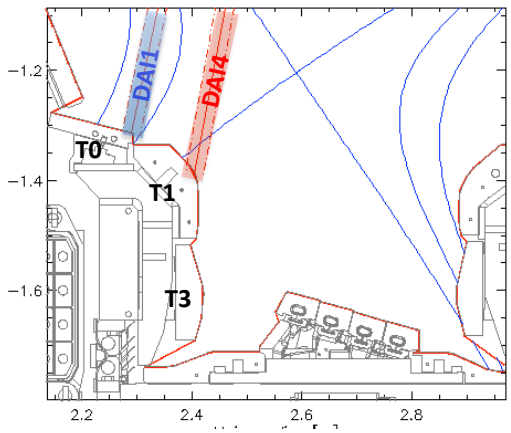

Figure A.6

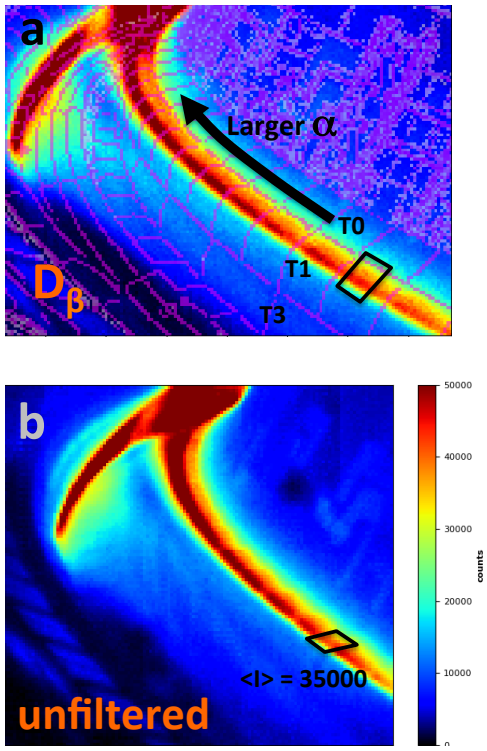

Figure A.7

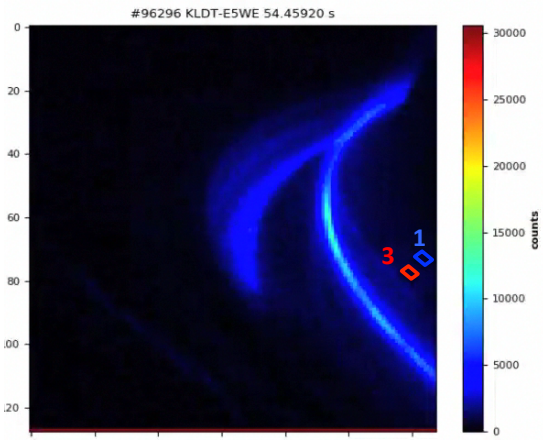

Figure A.8

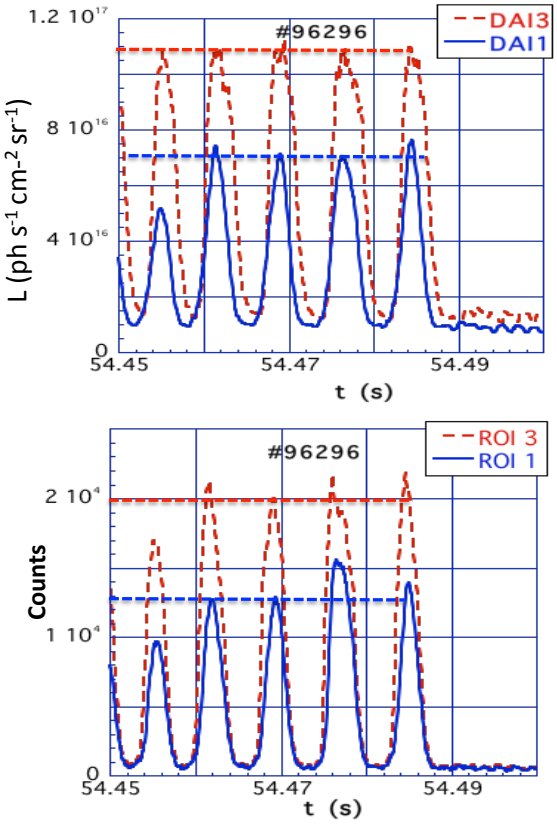

Figure A.9

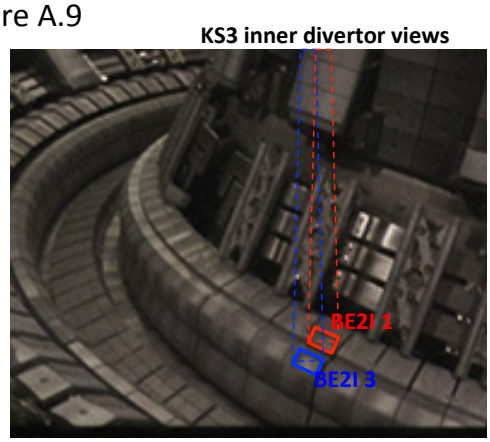

Figure A.10

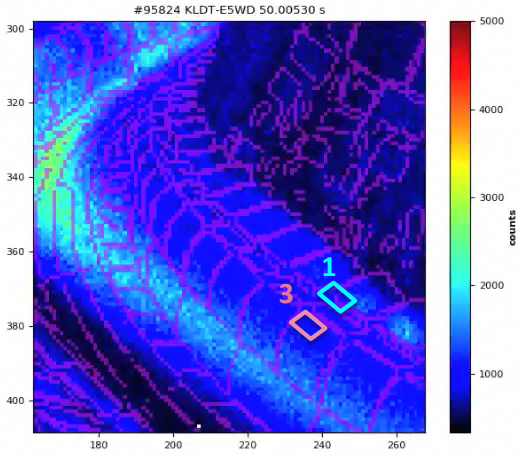

Figure A.11